JM PAPERS

# An experimental study of flow–structure interaction regimes of a freely falling flexible cylinder

Manuel Lorite-Díez[1], Patricia Ern[1,†], Sébastien Cazin[1], Jérôme Mougel[1] and Rémi Bourguet[1]

[1]Institut de Mécanique des Fluides de Toulouse (IMFT), Université de Toulouse and CNRS, France

The fluid–structure interaction problem composed of an elongated, finite-length, flexible cylinder falling in a fluid at rest is investigated experimentally. Tomographic reconstruction of the cylinder and three-dimensional particle tracking velocimetry of the surrounding fluid, based on the Shake-The-Box algorithm, are used jointly to capture both solid and fluid motions. Starting from the rectilinear vertical fall characterized by a steady wake, focus is placed on subsequent regimes involving, mainly in the horizontal direction, periodic rigid-body motions (RBM) of weak amplitude or periodic large-amplitude bending oscillations (BO). Two RBM regimes are explored: the TRA regime where the cylinder exhibits translational oscillations in a plane perpendicular to its axis, and the AZI regime in which the body displays an azimuthal oscillation around its centre. The associated unsteady wakes are composed of counter-rotating vortices bending near the body ends to connect with the adjacent vortex rows. Specific organizations of the vortical structures are uncovered, depending on the regime. In particular, in the AZI regime, they present an antisymmetrical distribution relative to the midspan point. For a sufficiently long cylinder, BO regimes emerge, resembling the structural modes of an unsupported beam. The associated wakes exhibit a cellular organization. Within each cell delimited by two deformation nodes, two counter-rotating vortex rows are shed per oscillation cycle. Flow velocity fluctuations are in phase opposition on each side of a deformation node. For both RBM and BO regimes, frequency and phase analyses of cylinder and wake behaviours, along the span, highlight the spatio-temporal synchronization of the unsteady flow and moving body.

Key words: wakes, flow–structure interactions, vortex shedding

† Email address for correspondence: ern@imft.fr

946 A16-1

## 1. Introduction

Bodies rising or falling freely in a fluid otherwise at rest display different styles of paths, such as rectilinear, oscillatory or chaotic, developing for specific ranges of the control parameters. Equally remarkable, they also exhibit periodic motions of contrasted amplitudes and frequencies, as well as periodic motions having different spatial symmetry properties, epitomized by planar zigzagging paths and spiralling paths (Ern *et al.* 2012). These different types of paths embody different types and strengths of coupling between the body and the fluid, as brought to the fore by studies based on numerical simulations and stability analysis of the fluid–body system. In particular, the emergence of contrasted paths, and of their associated wake structures, was investigated in the case of short-length cylinders ('disks' of variable thickness) by Auguste, Magnaudet & Fabre (2013), Chrust, Bouchet & Dušek (2013) and Tchoufag, Fabre & Magnaudet (2014), and for plates by Fabre, Assemat & Magnaudet (2011). These works revealed that shedding frequencies similar to the dominant frequency of the fixed-body wake are observed when fluctuations in the fluid exist without significant impact on the body motion. At variance, larger body oscillations emerge in association with fluttering or tumbling frequencies significantly different from the fixed-body wake frequency, and with specific wakes. At the same time, experimental investigations concerning the behaviour of freely moving bodies have been focused essentially on the solid-body kinematics, providing identifications and detailed characterizations of different body motions, as manifest in the latest works for rigid cylinders (Toupoint, Ern & Roig 2019), prolate and oblate spheroids (Will *et al.* 2021), and spheres (Kramer *et al.* 2021; Will & Krug 2021). As a consequence, the wake structures associated with these motions remain essentially unknown, when not also explored numerically. Yet recent advances in sophisticated optical techniques, enabling to achieve time-resolved simultaneous tracking in three dimensions of both body and fluid motions, have opened the way to the investigation, also experimentally, of both fluid and body behaviours and of their coupling; this is the route followed in the present paper.

Here, focus is placed on elongated finite-length circular cylinders (diameter $d$ and length $L$), as illustrated in figure 1. As one of the simplest three-dimensional geometries, circular cylinders have enabled the investigation of wake instability in situations of increasing complexity, in particular concerning the development of three-dimensional perturbations for infinitely long rigid cylinders fixed in flowing fluid (Karniadakis & Triantafyllou 1992; Zhang *et al.* 1995) or due to border effects for nominally two-dimensional wake flows about fixed cylinders (Williamson 1996). For finite-length cylinders fixed in an incoming fluid, the role of free ends was investigated numerically by Inoue & Sakuragi (2008), leading to the identification of different wake structures as the elongation ratio of the cylinder varies. A large stream of works also considered the introduction of degrees of freedom for the rigid cylinder, typically by mounting it on an elastic support, and investigated the properties of the vortex-induced vibrations (VIV) resulting from the balance between the hydrodynamical unsteady drag and lift forces experienced by the body and the restoring action of the structure (Sarpkaya 2004; Williamson & Govardhan 2004; Païdoussis, Price & De Langre 2010).

Freely moving cylinders, either rising or falling under the effect of buoyancy in fluid at rest, have received, however, little attention until now in comparison with other geometries. Two major features can be highlighted from the literature: the existence of various types of periodic paths, and the strong differences in amplitudes for these oscillatory motions. The coupling between wake instability and path oscillations for a freely falling/rising, infinitely long, rigid circular cylinder in an infinite fluid was investigated numerically by Namkoong, Yoo & Choi (2008). Focusing on Reynolds numbers ranging between 65 and 185, and
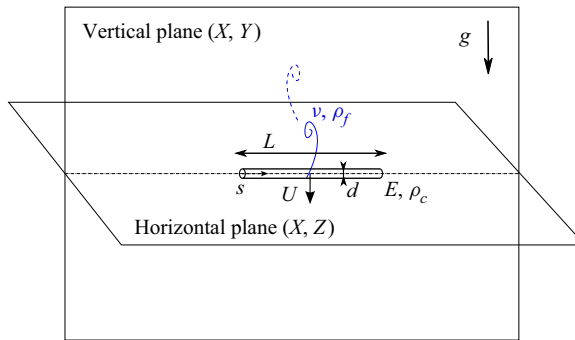
Figure 1. Sketch of the problem.

solid-to-fluid density ratios $m^*$ in the interval 0.5–4, they showed that the Bénard–von Kármán vortex street developing in the wake of the body couples to a low-amplitude periodic motion of the cylinder, in both translation and rotation, featuring transverse displacements typically less than $0.1d$ tending to delay vortex shedding. Paths displaying small-amplitude oscillations (typically $0.05d$) at a frequency close to the Bénard–von Kármán frequency were also found experimentally by Horowitz & Williamson (2006, 2010) for cylinders with two degrees of freedom in translation and one in rotation, in the same range of density ratios ($m^* > 0.54$) but higher Reynolds numbers ($3500 < Re < 7000$). In contrast, they observed large-amplitude oscillatory motions for lighter cylinders ($m^* < 0.54$) with displacement amplitudes of the order of $d$ in the transverse direction at a frequency approximately 1.3 times smaller (and of order $0.3d$ in the vertical direction at twice this frequency), in association with a wake structure comprising two vortex pairs generated per cycle. In the same configuration, Mathai *et al.* (2017) showed numerically that the rotational degree of freedom and $I^*$, the particle moment of inertia relative to that of the fluid, can influence the frequency and amplitude of motion, and change the wake shedding pattern from the two-single vortex mode to the two-pair vortex mode identified by Horowitz & Williamson (2010).

Different types of oscillatory motion are reported for finite-length rigid cylinders having free ends, and therefore six degrees of freedom. They supersede the steady rectilinear path in which the symmetry axis of the cylinder is perpendicular to the fall/rise velocity. Most investigations (Marchildon, Clamen & Gauvin 1964; Jayaweera & Mason 1965; Chow & Adams 2011; Romero-Gomez & Richmond 2016; Toupoint *et al.* 2019) focused on the two-dimensional periodic motion of the cylinder, called fluttering, existing for a wide range of control parameters and consisting of an angular oscillation of the symmetry axis relative to the horizontal (with typically an amplitude larger than $20°$ in Chow & Adams 2011) associated with significant periodic displacements of the centre of gravity. In this regime, the cylinder flutters with an amplitude of oscillation that decreases as the cylinder length increases, at given Reynolds number $Re$. Jayaweera & Mason (1965) mentioned further that the transition from steady fall to fluttering depends on $m^*$, and that the critical value of $Re$ above which fluttering occurs increases with increasing $L/d$; for steel cylinders with $L/d \simeq 10$, they found a critical value of $Re$ of approximately 50. Toupoint *et al.* (2019) also observed a strong dependence of the onset of path instability with $L/d$ in the range 2–20, but uncovered the existence of different oscillatory paths of weak amplitude in a transitional region separating the rectilinear and fluttering motions.

For freely moving finite-length cylinders, the knowledge of the wake structures associated with oscillatory paths is limited, to the authors' knowledge, to the dye

visualizations by Jayaweera & Mason (1965) and Toupoint *et al.* (2019). The latter revealed that a strong and regular vortex shedding activity in the cylinder wake is present in the case of the low-amplitude periodic paths. It is therefore particularly interesting to determine properly the specific properties of the wake structures associated with these motions. In the case of the fluttering motion, dye visualizations indicate more complex vortical structures, with eddies breaking away from both the edges and the sides of the cylinder, in particular during the gliding periods of the paths, as is known to occur for fluttering plates (Pesavento & Wang 2004; Andersen, Pesavento & Wang 2005; Lau *et al.* 2019); this case is therefore omitted from the scope of the present paper.

Besides the low-amplitude rigid-body motions described previously, this paper aims at identifying the wake structures tied to the bending oscillations occurring for freely falling flexible cylinders. Recently, Ern *et al.* (2020) found that the deformation modes of a flexible cylinder can be triggered during the cylinder free fall, when the structural frequencies are close to the wake frequency expected from the fixed-body configuration. The spatial and temporal properties of the wake structure associated with the cylinder motion and deformation, characterized by large-amplitude displacements (of the order of the cylinder diameter), are, however, unknown. Some insights can be gained from prior works concerning the related problem of the VIV of a flexible cylinder held from its ends and placed in flowing fluid (Chaplin *et al.* 2005; Bourguet, Karniadakis & Triantafyllou 2011*a*; Wu, Ge & Hong 2012; Fan *et al.* 2019). As in the case of elastically mounted rigid bodies (e.g. Williamson & Govardhan 2004), flexible cylinder VIV are driven by the synchronization between body motion and flow unsteadiness, which is associated with vortex formation in the wake. This mechanism of synchronization is often referred to as lock-in. For flexible bodies, frequency synchronization is accompanied by a coincidence of the spatial organization of the flow with body deformation. When the body is subjected to standing wave deformations, such a coincidence may result in cellular flow patterns (Bourguet 2020). The occurrence of lock-in, and its implications for the flow–body system behaviour, remain to be clarified for freely moving cylinders.

The purpose of the present paper is therefore to combine, experimentally, the analysis of the body responses with a detailed spatio-temporal description of the surrounding three-dimensional (3-D) flow, in distinct configurations featuring either periodic rigid-body motions of weak amplitude or large-amplitude bending oscillations of the cylinder. To capture fully the solid and fluid dynamics and their interaction, tomographic reconstruction is employed for the cylinder and time-resolved 3-D particle tracking velocimetry (PTV) based on the Shake-The-Box (STB) algorithm (Schanz *et al.* 2013; Schanz, Gesemann & Schröder 2016) for the fluid. As this technique generates massive data to be processed, it is presently hardly suitable for parametrical investigation. That is why contrasting paths reported in the literature for specific flow conditions were selected in order to uncover the vortical flow structures associated with them, and to investigate in detail their synchronization with the body motions. The selected cases are presented in the next section.

## 2. Physical system

When dropped in still fluid of density $\rho_f$ and kinematic viscosity $\nu$, a cylinder of length $L$, diameter $d$, density $\rho_c$ and Young's modulus $E$, falls/rises under the action of gravity $g$ and eventually settles at a falling/rising velocity $U$ after a transient. This problem is represented schematically in figure 1.

For a cylinder falling horizontally, i.e. without reconfiguration, as in the cases investigated here, the balance between the gravity force and drag acting on the body reads

| $d$ (mm) | $E$ (MPa) | $L$ (mm) | $m^*$ | $L/d$ | $Ar$ | $Ca$ | $U$ (mm s$^{-1}$) | $Re$ | $C_d$ | Regime |
|---|---|---|---|---|---|---|---|---|---|---|
| 1.12 | 1.02 | 39.5 | 1.16 | 35 | 47 | 2.6 | 44 | 49 | 1.41 | TRA |
| 1.02 | 1.02 | 57.0 | 1.16 | 56 | 40 | 15.5 | 41 | 42 | 1.48 | R |
| 1.09 | 1.02 | 74.5 | 1.16 | 68 | 45 | 36 | 39 | 42 | 1.79 | $M_1$ |
| 1.02 | 1.02 | 109.5 | 1.16 | 107 | 40 | 210 | 37 | 37 | 1.84 | $M_2$ |
| 1.90 | 1.02 | 19.0 | 1.16 | 10 | 103 | $O(10^{-2})$ | 65 | 124 | 1.09 | TRA |
| 0.80 | $O(10^3)$ | 32.0 | 1.16 | 40 | 28 | $O(10^{-3})$ | 39 | 31 | 1.31 | R |
| 2.55 | $O(10^3)$ | 51.0 | 1.16 | 20 | 161 | $O(10^{-4})$ | 85 | 217 | 0.86 | AZI |
| 2.70 | $O(10^3)$ | 27.0 | 1.16 | 10 | 175 | $O(10^{-5})$ | 96 | 259 | 0.72 | TRA |

Table 1. Cylinder characteristics, non-dimensional parameters and global variables for the selected cases. Cylinder density is the same for all cases, $\rho_c \simeq 1158.5\,\mathrm{kg\,m^{-3}}$. Water density and viscosity are $\rho_f = 1000\,\mathrm{kg\,m^{-3}}$ and $\nu = 1 \times 10^{-6}\,\mathrm{m^2\,s^{-1}}$, respectively. The gravitational acceleration $g$ is equal to $9.8\,\mathrm{m\,s^{-2}}$. Cylinders with $E \simeq 1.02\,\mathrm{MPa}$ are made of duplication silicone, and those with $E = O(10^3)$ are 3-D printed with ABS material.

$(\rho_c - \rho_f)g\pi d^2/4L = C_d d\rho_f U^2/2L$, where $C_d$ is the drag coefficient that depends on the cylinder aspect ratio and on the Reynolds number, defined as $Re = Ud/\nu$. This suggests a velocity scale associated to buoyancy, $V_g = \sqrt{(\rho_c/\rho_f - 1)gd}$, that will be used to define the non-dimensional parameters in this study.

The flow–structure system behaviour is governed by four dimensionless parameters:

(i) the solid-to-fluid density ratio, $m^* = \rho_c/\rho_f$;
(ii) the cylinder length-to-diameter ratio, $L/d$;
(iii) the Archimedes number, $Ar = V_g d/\nu$, which compares buoyancy and viscous effects and is classically used in free-fall studies; and
(iv) the Cauchy number, $Ca = (\rho_f V_g^2/E)(L/d)^4$, which can be interpreted as a ratio between fluid loads acting on the cylinder and bending stiffness forces, i.e. high $Ca$ values indicate that the body is susceptible to bend during its free fall – it can be noted that short enough cylinders may behave as rigid bodies, even if they are made of a soft material.

In the present study, the density ratio is constant and chosen slightly larger than unity ($m^* \simeq 1.16$), so that effectively, the cylinders fall. Wide ranges of $L/d$, $Ar$ and $Ca$ values are considered in order to cover a variety of behaviours of the flow–structure system. The general idea behind the selected parameter ranges was to examine further different regimes already reported in the literature (Toupoint *et al.* 2019; Ern *et al.* 2020) and complement prior shadowgraphy measurements and flow visualizations. The cases examined in this paper are presented in table 1, where the characteristics of each cylinder are reported together with the corresponding values of the non-dimensional parameters. Once the mean fall velocity $U$ of the cylinder is measured, the Reynolds number and drag coefficient, $C_d = (\pi/2)(V_g/U)^2$, can be obtained. The values of $U$, $Re$ and $C_d$ are indicated in table 1, as well as the regime names that will be defined in the following.

An overview of the $(Ar, L/d, Ca)$ parameter space under study is proposed in figure 2($a$). The cases examined in this paper are indicated by large circles, while those considered in Ern *et al.* (2020) for the same value of $m^*$ are denoted by small squares. The regimes of the flow–structure system are named in reference to the nature of the structural response, as explained hereafter. The colour code adopted to designate the different regimes is presented in figure 2($b$), where body response is depicted schematically for
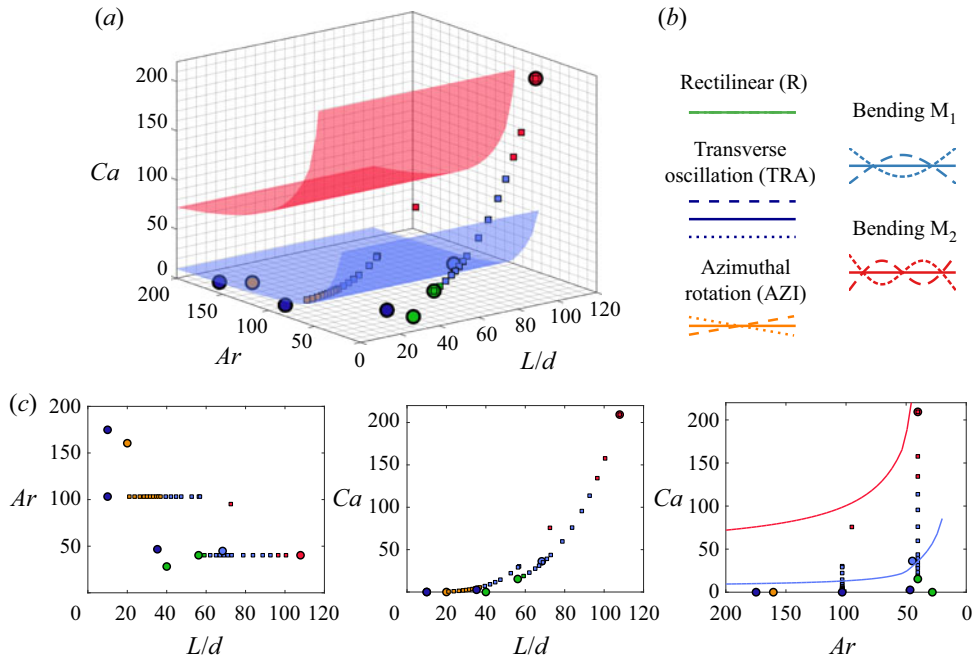
Figure 2. (*a*) Overview of the $(Ar, L/d, Ca)$ parameter space; the fourth non-dimensional parameter, the density ratio, is set to a constant value, $m^* = 1.16$. The cases examined in the present paper are denoted by large circles, and those reported in Ern *et al.* (2020) are indicated by small squares. The colour code employed to designate the different regimes is described in (*b*), where the associated structural responses in the horizontal $(X, Z)$ plane are schematized. (*c*) Two-dimensional projections of the parameter space. In (*a,c*), surfaces/lines represent the synchronization condition conjectured in Ern *et al.* (2020) for the emergence of the BO regimes (light blue for $M_1$, and red for $M_2$).

each regime. To ease visualization, two-dimensional projections of the parameter space are also plotted in figure 2(*c*).

Two main forms of structural responses of the freely falling cylinder are examined in this paper. They are associated with two distinct groups of regimes: (i) rigid-body motion (RBM) regimes where the cylinder falls without significant unsteady deformation, and (ii) bending oscillation (BO) regimes. The different regimes share a common feature, i.e. essentially, possible cylinder oscillatory motion occurs in the horizontal plane.

Three RBM regimes are investigated. The rectilinear (R) regime (green symbols) corresponds to a steady rectilinear fall of the body. Its possible oscillations are of the same order of magnitude as the ambient noise and close to measurement precision. The falling cylinder may also exhibit translatory and rotary responses, which are associated with the transverse (TRA) and azimuthal (AZI) oscillation regimes, respectively; these regimes are depicted by dark blue and orange large circles in figure 2(*a,c*). The RBM regimes are encountered principally in the lower range of *Ca* values, which is consistent with the fact that fluid forces are not able to bend the cylinder. The RBM regimes can, however, arise for rather flexible bodies, e.g. the R regime for $Ca = 15.6$, the TRA regime for $Ca = 2.64$, or the AZI regime for $Ca \in [0.57, 5.33]$. The R regime is observed for low *Ar* (and *Re*) values. The cases of TRA and AZI regimes correspond to relatively short cylinders, over a wide range of *Ar* values.

**946** A16-6

The BO regimes were uncovered in a prior work based on shadowgraphy measurements of body responses (Ern *et al.* 2020). The vibration patterns associated with these regimes resemble the structural modes of an unsupported beam, and they were named accordingly, i.e. the $M_i$ regime corresponds to the *i*th mode. The $M_1$ and $M_2$ regime cases are denoted by light blue and red large circles in figure 2; a typical example of each regime will be examined in the present paper (table 1). In the previous study, it was conjectured that such regimes develop when the frequency of flow unsteadiness, associated with vortex shedding, is close to a natural frequency of the body, leading to flow–body synchronization or lock-in. A simple condition for the *i*th bending mode to be excited by the flow has been proposed: $f_w = f_i$, where $f_w$ is the vortex shedding frequency and $f_i$ is the natural frequency of the *i*th bending mode.

Using a linear Euler–Bernoulli beam equation with free ends conditions to model the solid dynamics, and a potential added-mass coefficient of 1, the natural frequency of the *i*th mode can be expressed as $f_i = \alpha_i d/L^2 \sqrt{E/(\rho_c + \rho_f)}$, where $\alpha_1 \approx 0.890$, $\alpha_2 \approx 2.454$, $\alpha_3 \approx 4.811$, etc. Considering the non-dimensional vortex shedding frequency, referred to as the Strouhal number $St = f_w d/U$, and assuming that $U = V_g$ (i.e. $C_d = \pi/2$, which is valid roughly for large $L/d$ in the investigated range of *Re*; Ern *et al.* 2020), the above synchronization condition becomes $C_a = (1 + m^*)^{-1}(\alpha_i/St)^2$. Assuming that the end effects are negligible (i.e. long enough cylinders), the Strouhal number depends on *Ar* (or *Re*, equivalently, since $U = V_g$) only, and can be modelled (neglecting cylinder vibration effects) based on prior tabulated results (e.g. Williamson & Brown 1998; Buffoni 2003). Under these assumptions, for a given mode and a given value of $m^*$, the above condition is independent of $L/d$ and corresponds to the surfaces/lines plotted in figure 2(*a,c*), for the first (light blue) and second (red) bending modes. In spite of the underlying assumptions, these surfaces/lines match globally the experimental observations and provide an estimate of the BO regime locations in the parameter space.

It should be recalled that the conjecture of synchronization associated, in the above-mentioned study (Ern *et al.* 2020), with the appearance of the BO regimes, was hypothesized from structural response shapes and frequencies. In general, as noted previously, the RBM and BO regimes reported in this section have been identified in Toupoint *et al.* (2019) and Ern *et al.* (2020), where they were described essentially on the basis of cylinder motion measurements. The associated flow features and flow–structure interaction mechanisms remain to be explored. An attempt is made in this paper via time-resolved 3-D PTV, i.e. a joint quantitative measurement of body and flow dynamics. The experimental procedure is presented in the next section.

## 3. Experimental methodology

The principal aspects of the experimental procedure are presented in this section. The experimental set-up is described in § 3.1. The strategy employed to determine the dynamics of the body and 3-D flow surrounding it is explained in § 3.2. Some elements concerning the analysis of the structural dynamics – i.e. filtering and frame change – are reported in § 3.3. Additional details of the experimental method are presented in Appendix A.

### 3.1. *Set-up*

The experiments are carried out in a water tank whose cross-section is $0.25\,\mathrm{m} \times 0.25\,\mathrm{m}$. The tank is filled with distilled water up to height $0.6\,\mathrm{m}$. A simplified sketch of the experimental set-up is presented in figure 3. The cylinder characteristics are detailed in
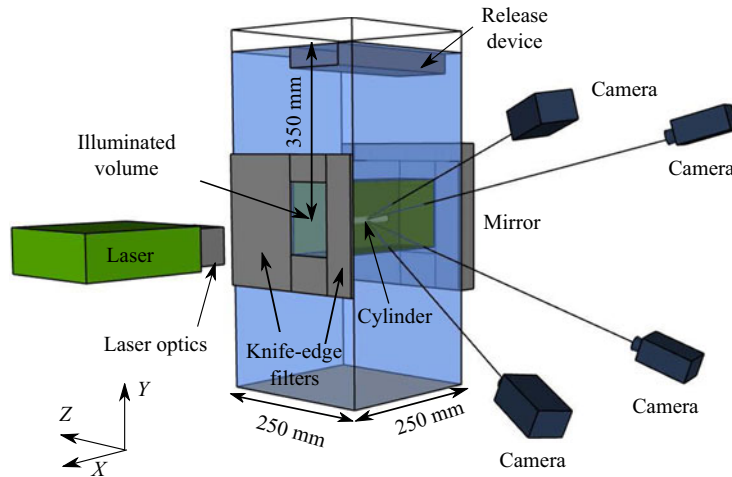
Figure 3. Sketch of the experimental set-up.

table 1. Tank temperature is kept at 20 °C in order to keep constant water density, viscosity and refractive index.

Although the phenomena examined here are independent from the initial conditions, as shown by Toupoint *et al.* (2019) and Ern *et al.* (2020), the limited measurement volume requires a robust procedure for cylinder release. In that sense, an automatic device is used to ensure a repeatable and accurate drop of the cylinders. The device consists of two arrays of pins aligned in two perpendicular planes. The horizontal array of pins holds the cylinder below the free surface to avoid the presence of bubbles on the cylinder. The vertical array, which is controlled pneumatically, can be translated to carefully push and release the cylinder at the top of the tank.

A 527 nm, $2 \times 60$ mJ-per-pulse laser from Photonics Industries (ref. DM60-527-DH) is used to illuminate the seeding particles and the slightly fluorescent cylinder within the measurement volume. In order to light a delimited 3-D volume in the middle of the tank, an optical device (LaVision GmbH Volume Optics Module) expands the collimated laser beam. The sharp boundaries of this volume are delimited by knife-edge filters (see figure 3). A mirror is placed on the other side of the tank to increase the illumination in the volume. This double-pass illumination system increases the efficiency of the illumination by approximately 50 % (Scarano 2012).

The images are captured by four high-speed VEO640 Phantom cameras (equipped with 200 mm F/11 Nikon lenses) placed on a bench, at 100 cm from the frontal face of the tank. The cameras are set in a square-shaped arrangement; the distance between consecutive camera lenses is 67 cm. All the cameras are tilted by approximately 20° horizontally and vertically, towards the experiment. Respecting the Scheimpflug conditions, the lines of sight of the cameras are directed towards the centre of the illuminated volume. The emission peak of the seeding particles is located at approximately 568 nm. To avoid reflections from the laser beam on the cylinder, the camera lenses are equipped with optical high-pass filters (540 nm).

The fluorescent seeding particles are polyamide covered with rhodamine B; their diameter is close to 22 μm, and their density is $\rho_p \approx 1030$ kg m$^{-3}$. For a typical experiment, the solute particles are introduced in the tank at several heights and then mixed to ensure their homogeneous distribution. The experiment is started 20 min after that.

Following this procedure, the particle density, expressed in p.p.p. for particles per pixel (see Scarano 2012), ranges from 0.02 to 0.025 p.p.p.

The coordinate system $(X, Y, Z)$, related to the experimental set-up, is defined as shown in figures 1 and 3. The illuminated measurement volume has been defined by a 3-D calibration procedure detailed in § A.1. It has size $(\Delta X_v, \Delta Y_v, \Delta Z_v) = (132, 86, 35)$ mm, corresponding typically to $13d$–$35d$ in the horizontal direction and $48d$–$130d$ in the vertical one. The volume is located at mid-height of the tank, at distance 350 mm from the free surface; this location ensures that the permanent behaviour of the falling cylinder is reached, and also avoids any influence from the bottom wall. As indicated by previous measurements (Ern *et al.* 2020), the vertical extent of the present measurement volume, $Y_v$, is long enough to capture several periods of body oscillation, in most cases. The $X_v$ extent has been chosen to capture fully the longest cylinder, i.e. $L = 110$ mm. The choice of $Z_v$ is a compromise between the typical width of cylinder wakes and the intensity of the seeding particles illumination.

The seeding particles located between the measurement volume and the front wall of the tank cause turbidity. Turbidity effect is actually small, but to further reduce it, the measurement volume is placed closer to the tank front wall. It has been verified that the distance from the wall remains sufficient to avoid any spurious interaction with the falling cylinder; the distance between the body and the wall is larger than $10d$ even in the worst case.

### 3.2. *Capture of fluid and body motions*

The Shake-The-Box (STB) method is employed to capture the spatio-temporal evolution of the 3-D flow surrounding the cylinder, while the body dynamics is determined via tomographic reconstruction.

The STB method relies on a particle tracking algorithm that consists in predicting the seeding particle distribution within the flow field by extrapolating past known trajectories; it is designed to use as much temporal and spatial information from the acquired images as possible. It combines several tools, in particular the 3-D volume self-calibration of TOMO-PIV (Wieneke 2008) and the optical transfer function (OTF) (Schanz *et al.* 2012), as well as the iterative particle reconstruction (IPR) method for volumetric particle distribution (Wieneke 2012).

In comparison with other techniques, the STB method can be applied to particle densities comparable to the standard TOMO-PIV (typically around 0.05 p.p.p.), i.e. much higher than other 3-D PTV techniques (Schanz *et al.* 2013). The spatial resolution of the STB method is higher than that reached via TOMO-PIV, since the algorithm is based not on the intercorrelation of volume elements containing several particles but on the 3-D tracking of individual particles. The required computational and memory resources are also reduced; this is an important aspect considering the amount of data to be processed. Using the predicted positions of the particles (STB concept), combined with a minimum track-length criterion, solves the problem of ghost particles, which is an important issue in other tomographic approaches (due to the existence of multiple optical solutions for a given particle position). Furthermore, in the present configuration, the standard TOMO-PIV algorithm would have correlated cylinder displacements in some interrogation windows close to the body, producing velocity vectors that do not relate to seeding particle motion.

In a typical experiment, $4 \times 2000$ images ($2560 \times 1600$ pixels) are recorded at 500 Hz, which covers the entire displacement of the cylinder across the measurement volume (500–1000 images, depending on $d$). The images are recorded and processed (calibration,

STB and tomographic reconstruction) using DaVis 10.1 software by LaVision GmbH. The first crucial steps correspond to image pre-processing and volume self-calibration, as detailed in § A.1. Image analysis can then be carried out to determine the flow field via the STB method and to extract the cylinder dynamics using tomographic reconstruction. Details concerning the parameters of the STB computation on the seeding particles are reported in § A.2. The procedure followed for tomographic reconstruction from individual views of the cylinder provided by the four cameras is described in § A.3.

Once the particle tracking algorithm establishes the motion of each seeding tracer in the fluid, the particle trajectories are smoothed using a cubic spline to remove the noise induced by derivative computation and therefore obtain appropriate velocity and acceleration values (this procedure is included in the DaVis software). In order to cover long enough particle displacement in each track and retain the maximum level of details, the filter length has been adapted depending on the cylinder falling velocity.

To compute the spatial derivatives of flow quantities and to ease the presentation of some results, the data issued from the STB method have been interpolated on a regular grid by a binning operation via DaVis. The binning consists in interpolating the quantities associated with the particles located inside a grid element (bin) at a given instant. The mesh considered for the interpolation is a regular grid composed of $56 \times 56 \times 56$ voxels, with an overlap of 87.5 %. A linear interpolation that requires only one particle per grid element is employed. The spatial resolution associated with this grid is 0.32 mm in each direction; as shown in the following, such resolution is sufficient to capture the principal 3-D vortical structures developing in the cylinder wake, whose typical size is larger than the cylinder diameter.

In addition to binning interpolation, the particle tracks issued from the STB method can also be used directly to characterize the recirculation region appearing in the near wake of the cylinder. To do so, all particle trajectories are captured during a given experiment in a spanwise region of 4 mm width, typically close to the midspan point. Then the recirculation region is identified based on the relative velocity of the particles with respect to the cylinder, which is time-averaged and space-averaged over this spanwise region.

### 3.3. *Processing of cylinder dynamics*

The different steps of post-processing applied to the cylinder motion data are described in the following.

Figure 4(*a*) depicts a typical trajectory of the cylinder centre of mass for each regime examined in this work; the position of the centre of mass expressed in the $(X, Y, Z)$ frame is denoted by $(X_{CM}, Y_{CM}, Z_{CM})$. In all cases, the body exhibits a slight, non-reproducible, lateral drift. Such weak deviations have been reported previously in experiments concerning comparable physical systems (e.g. Fernandes *et al.* 2007; Toupoint *et al.* 2019). No preferential direction of the lateral drift emerged, confirming that the release procedure had no significant influence on the results. Its magnitude is small (lower than 3 % of the vertical velocity $U$), so the cylinder fall is close to vertical, in all studied cases.

Erratic fluctuations of low magnitude are also visible on the cylinder paths, in particular in the regimes where the cylinder centre of mass is not expected to oscillate, e.g. the R and AZI regimes (figure 4*a*). They are of the same order of magnitude as the experimental noise, and close to measurement precision; they may be attributed to slight imperfections in the experimental procedure. Finally, in the TRA and BO regimes, the centre of mass exhibits regular oscillations superimposed on the weak lateral drift and on the erratic
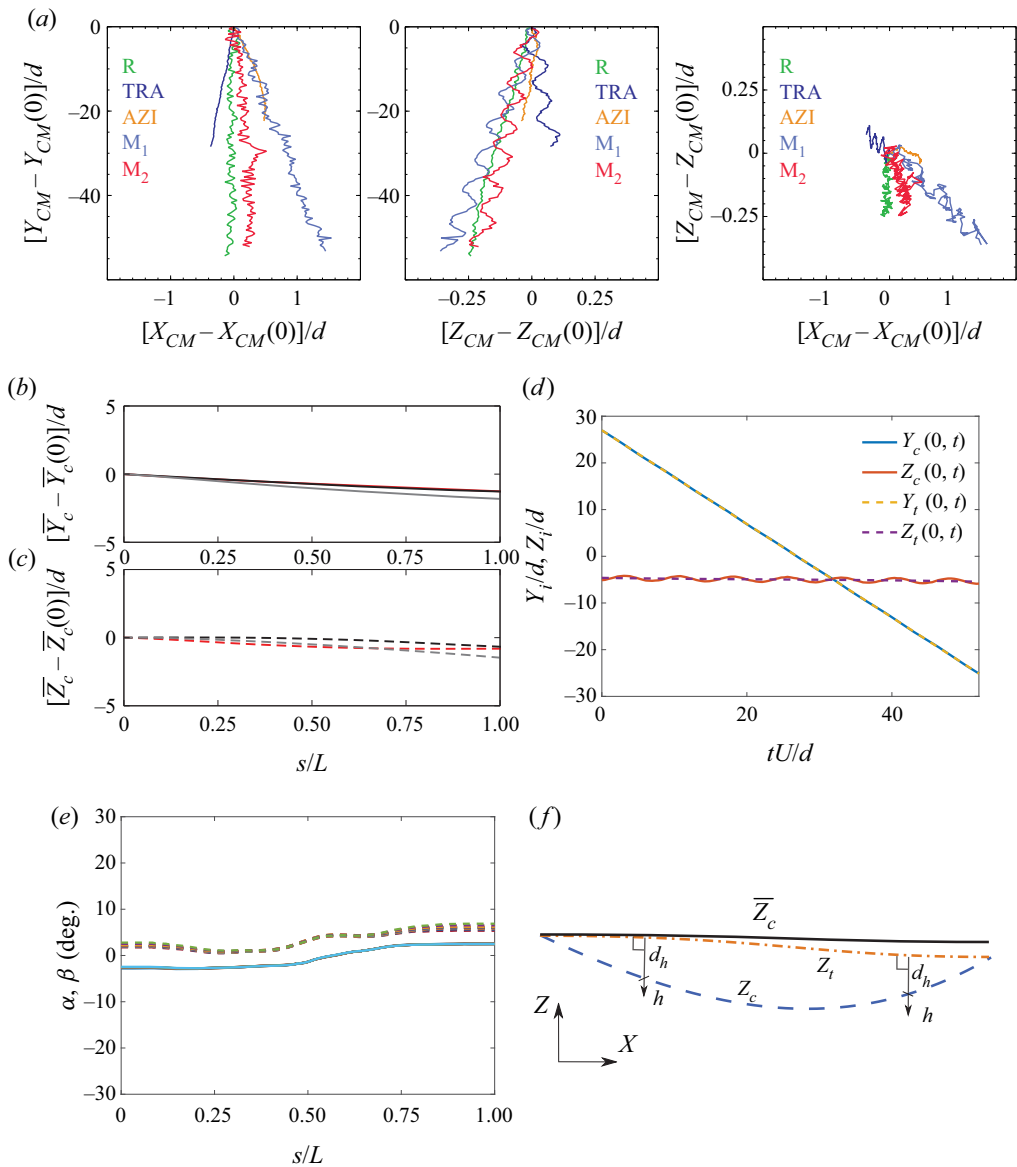
Figure 4. (*a*) Examples of trajectories of the cylinder centre of mass for the different regimes under study: R ($Ar \simeq 40$, $Re \simeq 42$, $Ca \simeq 15.5$, $L/d \simeq 56$), TRA ($Ar \simeq 103$, $Re \simeq 124$, $Ca = O(10^{-2})$, $L/d \simeq 10$), AZI ($Ar \simeq 161$, $Re \simeq 217$, $Ca = O(10^{-4})$, $L/d \simeq 20$), $M_1$ ($Ar \simeq 45$, $Re \simeq 42$, $Ca \sim 36$, $L/d \simeq 68$) and $M_2$ ($Ar \simeq 40$, $Re \simeq 37$, $Ca \sim 210$, $L/d \simeq 107$). The colour code is the same as in figure 2. The coordinates are centred about the initial position ($X_{CM}(0)$, $Y_{CM}(0)$, $Z_{CM}(0)$). The three plots correspond to projections of the paths in two vertical planes and a horizontal plane. (*b*,*c*) Time-averaged displacements in the (*b*) $Y$ axis and (*c*) $Z$ axis directions, along the cylinder span, for three successive experiments concerning the $M_1$ regime; $\bar{Y}_c$ and $\bar{Z}_c$ are centred about the $s = 0$ values. (*d*) Time evolution of the cylinder instantaneous position ($Y_c$, $Z_c$) and trend ($Y_t$, $Z_t$) at $s/L = 0$ ($M_2$ regime). (*e*) Local inclination angles $\alpha$ (solid lines) and $\beta$ (dashed lines), along the span, every $\Delta tU/d \approx 4.3$, for a typical experiment concerning the $M_2$ regime. (*f*) Sketch of the frame attached to the trend of the falling body: $h$ direction and $d_h$ displacement in the horizontal plane, at a given instant.

fluctuations of lower magnitude. While these oscillations are expected in the TRA and $M_1$ regimes, in the case of $M_2$ (the longest cylinder), the oscillation of the cylinder centre of mass should be, ideally, close to 0. The oscillations observed may result from slight asymmetries in the cylinder geometry.

A local non-inertial frame of reference is introduced in order to quantify the horizontal and vertical responses of the cylinder. The curvilinear abscissa $s$ follows the instantaneous cylinder axis, as illustrated in figure 1, and ranges from 0 to $L$ (i.e. body length, which does not vary during the fall). The coordinates of each point of the cylinder in the $(X, Y, Z)$ frame are denoted by $(X_c(s, t), Y_c(s, t), Z_c(s, t))$, where $t$ represents the time variable. The time-averaged values of $Y_c$ and $Z_c$ are plotted along the span in figure 4($b$,$c$), for three successive experiments concerning the $M_1$ regime; in these plots and in the following, a bar designates the time-averaged value. The time-averaged coordinates represented in the plots are centred about the time-averaged position of the body at $s = 0$. These examples show that the cylinder does not undergo any significant static reconfiguration during its fall, and that the mean position of its axis remains globally aligned with the $X$ axis.

A detrend procedure is applied in order to describe the cylinder vibrations. The objective is to distinguish the instantaneous local oscillations of the body from its mean or slowly-evolving behaviour/trend, i.e. involving time scales that are one or more orders of magnitude larger. The main trend of cylinder position evolution is captured, at each spanwise location, by applying a Savitzky–Golay filter (third-order polynomial; Savitzky & Golay 1964) to the instantaneous position, over the entire time series. The trend of cylinder displacements expressed in the $(X, Y, Z)$ frame is denoted by $(X_t(s, t), Y_t(s, t), Z_t(s, t))$, where the subscript $t$ refers to the time-dependent nature of the trend.

By changing the filter operator (e.g. moving average) and the present filter properties (order, window), it has been verified that the selected filter has no substantial impact on the results; this can be explained by the difference in the typical time scales of body drift and vibrations. The detrend procedure is illustrated in figure 4($d$) for a typical case of the $M_2$ regime, at $s = 0$.

The global alignment of the time-averaged cylinder position with the $X$ axis is actually observed at each time instant, as illustrated in figure 4($e$), which represents the spanwise evolution of the inclination angles $\alpha$ and $\beta$, at several instants ($M_2$ regime case); the inclination angles denote the local deviations of the trend $(X_t, Y_t, Z_t)$ from the $(X, Y)$ and $(X, Z)$ planes, i.e. the vertical plane of release and the horizontal plane, respectively. Both angles remain close to $0°$ along the span: the body falls in the horizontal plane and does not significantly rotate relative to its release position. This has been verified in all studied cases.

The horizontal ($h$) and vertical ($v$) directions normal to the trend of the falling body are defined, locally and instantaneously, as follows: $h$ is the direction normal to the trend and parallel to the $(X, Z)$ plane, while $v$ is the direction normal to the trend and parallel to the $(X, Y)$ plane. At each time instant $t$ and each spanwise location $s$, the displacement $d_h(s, t)$ ($d_v(s, t)$, respectively) represents the distance between the trend and the actual position of the cylinder along the $h$ axis ($v$ axis, respectively). A sketch of the instantaneous horizontal direction $h$ and corresponding displacement $d_h$ at a given instant is proposed in figure 4($f$). Therefore, the flow features can be depicted in the $(s, v, h)$ coordinate system, defined relative to the cylinder, taking into account the local and instantaneous orientation of the cylinder during its fall. In that way, averaged flow fields can be computed in this coordinate system.

The frequency content of the structural responses and the flow is determined via fast Fourier transform of the corresponding time series. The amplitudes of the structural responses are the instantaneous envelopes of $d_h$ and $d_v$, denoted by $A_h$ and $A_v$ in the following, which are obtained through the Hilbert transform of $d_h$ and $d_v$ time series.

## 4. Rigid-body motion regimes

As mentioned previously, the objective here is not to present a parametrical study across the $(Ar, L/d, Ca)$ parameter space, but to further investigate the regimes identified on the basis of structural responses in prior works. To do so, typical cases, representative of each regime, have been selected within this parameter space (table 1). In this section, focus is placed on the RBM regimes. For each regime (R, TRA and AZI), body responses are examined in § 4.1, wake patterns are described in § 4.2, and flow–structure interaction mechanisms are analysed in § 4.3.

### 4.1. *Structural responses*

The results reported in the following aim to complement some previous observations and shed additional light on the spatio-temporal properties of the responses, which will be connected to flow dynamics in § 4.3.

The typical amplitudes, frequency content and phasing of cylinder responses in the three RBM regimes are depicted in figure 5. The rectilinear (R) regime – identified previously in this parameter range by Ern *et al.* (2020) and observed here for cylinders with different Young's modulus (table 1) – is characterized by non-reproducible, irregular responses of very low amplitudes ($\overline{\langle A_{h,v} \rangle} < 0.01$), close to the experimental noise/precision limit; recall that $\langle \rangle$ designates the span-averaged value and the bar the time-averaged value. No frequency peak emerges in response spectra (figure 5*b*).

The response amplitudes encountered in the transverse (TRA) and azimuthal oscillation (AZI) regimes are larger than in the R regime but remain lower than 0.05 body diameters. These amplitudes are one order of magnitude lower than those reported for the vortex-induced vibrations of elastically mounted rigid cylinders at comparable $Re$ values (Singh & Mittal 2005), but comparable to those observed for two-dimensional freely moving cylinders (Namkoong *et al.* 2008). The horizontal oscillation amplitudes are substantially larger than the vertical ones, i.e. body oscillations are restricted mainly to the horizontal plane. Such a difference between horizontal and vertical response magnitudes has been observed in previous works concerning freely moving bodies (Ern *et al.* 2012) and elastically mounted bodies (Singh & Mittal 2005). Considering the limited amplitudes of the vertical responses (close to the experimental precision limit), the present analysis focuses on the horizontal oscillations.

The TRA regime presents reproducible displacements of constant amplitudes along the span, $\overline{A_h} \approx \langle \overline{A_h} \rangle \approx 0.03$. The motion is close to periodic and dominated by a single frequency, as illustrated by the span-averaged spectrum in figure 5(*b*). The dominant frequency matches that measured via shadowgraphy for longer time series (red dashed-dotted line); this confirms the accuracy of the solid reconstruction approach described in § A.3. In this spectrum, the peak occurs close to $fd/U = 0.12$, which is reminiscent of the vortex shedding frequency past a stationary cylinder of comparable aspect ratio (figure 7 in Inoue & Sakuragi 2008); this point will be discussed further in the following. The spanwise evolution of the phase associated with the dominant oscillation frequency is plotted in figure 5(*c*), for two typical cases of the TRA regime. In this plot, the
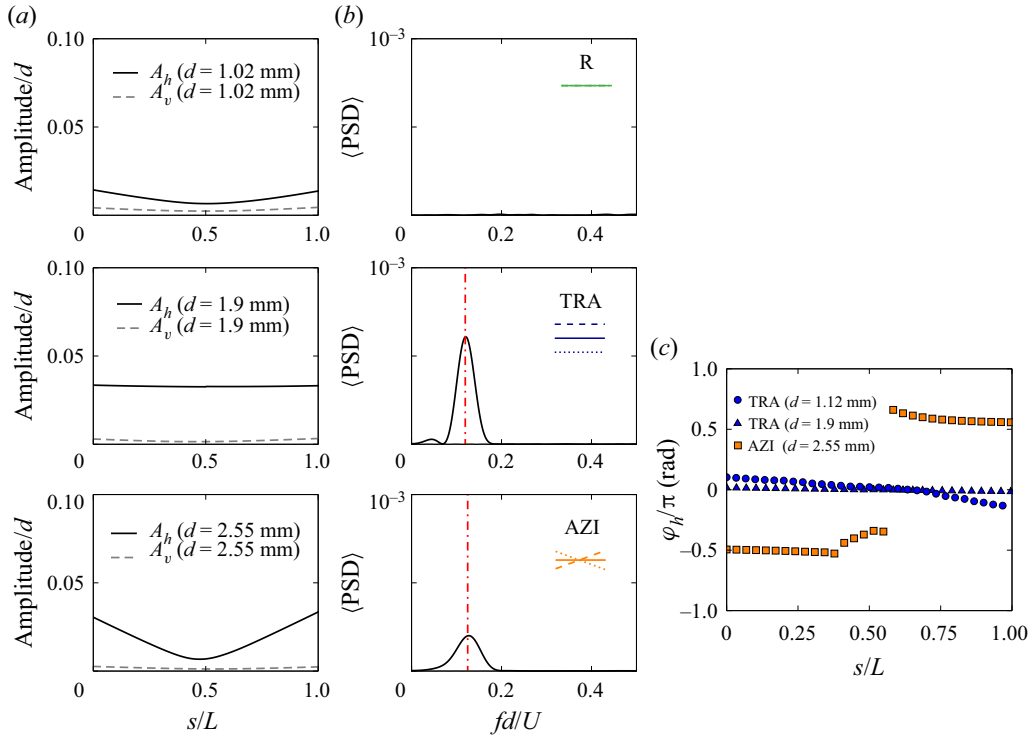
Figure 5. Structural responses in the RBM regimes. (*a*) Spanwise evolution of the time-averaged amplitude of oscillation and (*b*) span-averaged frequency spectrum (PSD) of the oscillation, in the horizontal (plain line) and vertical (dashed line) directions, in the R ($Ar \simeq 40$, $Re \simeq 42$, $Ca \simeq 15.5$, $L/d \simeq 56$, top), TRA ($Ar \simeq 103$, $Re \simeq 124$, $Ca = O(10^{-2})$, $L/d \simeq 10$, middle) and AZI ($Ar \simeq 161$, $Re \simeq 217$, $Ca = O(10^{-4})$, $L/d \simeq 20$, bottom) regimes. In (*b*), the oscillation frequencies reported in Ern *et al.* (2020) based on shadowgraphy experiments, for the same cylinders, are indicated by red dashed-dotted lines. (*c*) Spanwise evolution of the phase associated with the dominant frequency of the horizontal oscillation in the TRA ($d = 1.12$ mm, $Ar \simeq 47$, $Re \simeq 49$, $Ca \simeq 2.6$, $L/d \simeq 35$; $d = 1.9$ mm, $Ar \simeq 103$, $Re \simeq 124$, $Ca = O(10^{-2})$, $L/d \simeq 10$) and AZI ($d = 2.55$ mm, $Ar \simeq 161$, $Re \simeq 217$, $Ca = O(10^{-4})$, $L/d \simeq 20$) regimes; the phases are centred about their span-averaged values, and two cases of the TRA regime are considered.

phases $\varphi_h$ are centred about their span-averaged values, i.e. $\langle \varphi_h \rangle$. For each case, response phase remains relatively constant along the span, as expected for a transverse rigid-body oscillation.

The typical amplitudes of the structural oscillations observed in the AZI regime are comparable to those encountered in the TRA regime, except that their magnitude varies along the span and reaches a minimum value at the midspan point (figure 5*a*). As in the TRA regime, a single frequency dominates the spectrum of these responses, which remain close to periodic. Due to the high fall velocity in the case visualized in figure 5(*a*,*b*) (table 1), only a few oscillation cycles are captured within the measurement volume. This explains the relatively wide frequency peak; it can, however, be noted that the dominant frequency matches that issued from shadowgraphy (red dashed-dotted line), close to $fd/U = 0.12$, as in the above TRA regime case. As expected due to the rotary nature of the AZI regime, the response phase switches by $\pi$ close to the midspan point, i.e. cylinder ends are in phase opposition (figure 5*c*).

**946** A16-14

### 4.2. *Flow patterns*

A first overview of the typical wakes associated with the three RBM regimes is proposed in figure 6, through instantaneous iso-surfaces of the $\lambda_2$ criterion (Jeong & Hussain 1995), coloured by iso-contours of the spanwise vorticity (*s* component). Illustrations including wake and cylinder dynamics are also available as supplementary movies 1, 2 and 3 available at https://doi.org/10.1017/jfm.2022.540.

The R regime is encountered at low Reynolds numbers, within the subcritical range where the flow past a rigidly mounted cylinder is expected to be steady in the absence of end effects (Williamson 1996). As discussed in § 5.2, the addition of degrees of freedom to the body may cause flow unsteadiness to appear below the critical *Re* value of 47. This is not the case here. No vortex shedding is observed downstream of the cylinder (left-hand plot of figure 6*a*). The flow is found to be steady and remains essentially symmetrical about the $(s, v)$ plane. This is illustrated further in the right-hand plot of figure 6(*a*) by a visualization of the flow surrounding the cylinder based on STB trajectories of the seeding tracers.

In the TRA regime, the flow is unsteady and composed of well-defined vortical structures shed downstream of the body. The shape of the vortical structures involved in this regime varies with $L/d$ and *Re*, as shown in figure 6(*b*). For the cylinder of aspect ratio $L/d = 35$, the alternating vortices are parallel to the body axis and present a nearly two-dimensional pattern along most of the span. The spanwise invariance of the vortices ceases near the body ends, where they are bent and connected to the adjacent vortex rows. The region of spanwise invariance tends to vanish when cylinder aspect ratio is reduced, as illustrated in figure 6(*b*) for $L/d = 10$. In this case, the vortices resemble hairpin structures. Similar hairpin structures were reported by Inoue & Sakuragi (2008) downstream of stationary low-aspect-ratio cylinders at comparable *Re* values. The transition between the above-mentioned nearly two-dimensional structures and the hairpin structures appears to be continuous: as the cylinder aspect ratio increases, the spanwise region of the hairpin vortex that is parallel to the body axis widens, leading to an area of parallel shedding. In that sense, the parallel shedding pattern could be regarded as a spanwise-extended version of the hairpin pattern.

The two selected cases of the TRA regime for which $L/d = 10$ in figure 6(*b*) exhibit comparable structural responses and are both characterized by hairpin vortex wakes. They differ essentially by their *Re* value, 124 versus 259. It can be noted that the instantaneous vortex shape becomes less regular as *Re* increases (the $\lambda_2$ criterion value is the same in both cases); the appearance of such small-scale erratic modulations coincides with the emergence of three-dimensionality of the spanwise vortex rows downstream of a large-aspect-ratio cylinder, close to $Re = 180$ (e.g. Williamson 1996). Regardless of the parallel or hairpin shape of the vortices encountered in the TRA regime, the formation and detachment of each vortex from the cylinder seem to occur simultaneously on each side of the body (in the *s* direction, i.e. $s/L < 0.5$ versus $s/L > 0.5$); such symmetry in the unsteady flow patterns will be examined in § 4.3.

The typical unsteady wake associated with the AZI regime is depicted in figure 6(*c*). It is composed mainly of curved spanwise vortices that represent an intermediate state between the parallel and hairpin vortex patterns described previously in the TRA regime. Such an intermediate pattern is expected, considering the intermediate value of the aspect ratio ($L/d = 20$). Similar patterns have been reported for comparable aspect ratios by Inoue & Sakuragi (2008) (stationary cylinder) and Toupoint *et al.* (2019) (freely moving cylinder); it also resembles the oblique shedding pattern described by Williamson (1989). The value of the Reynolds number in the selected case of the AZI regime, $Re = 217$, is close to the
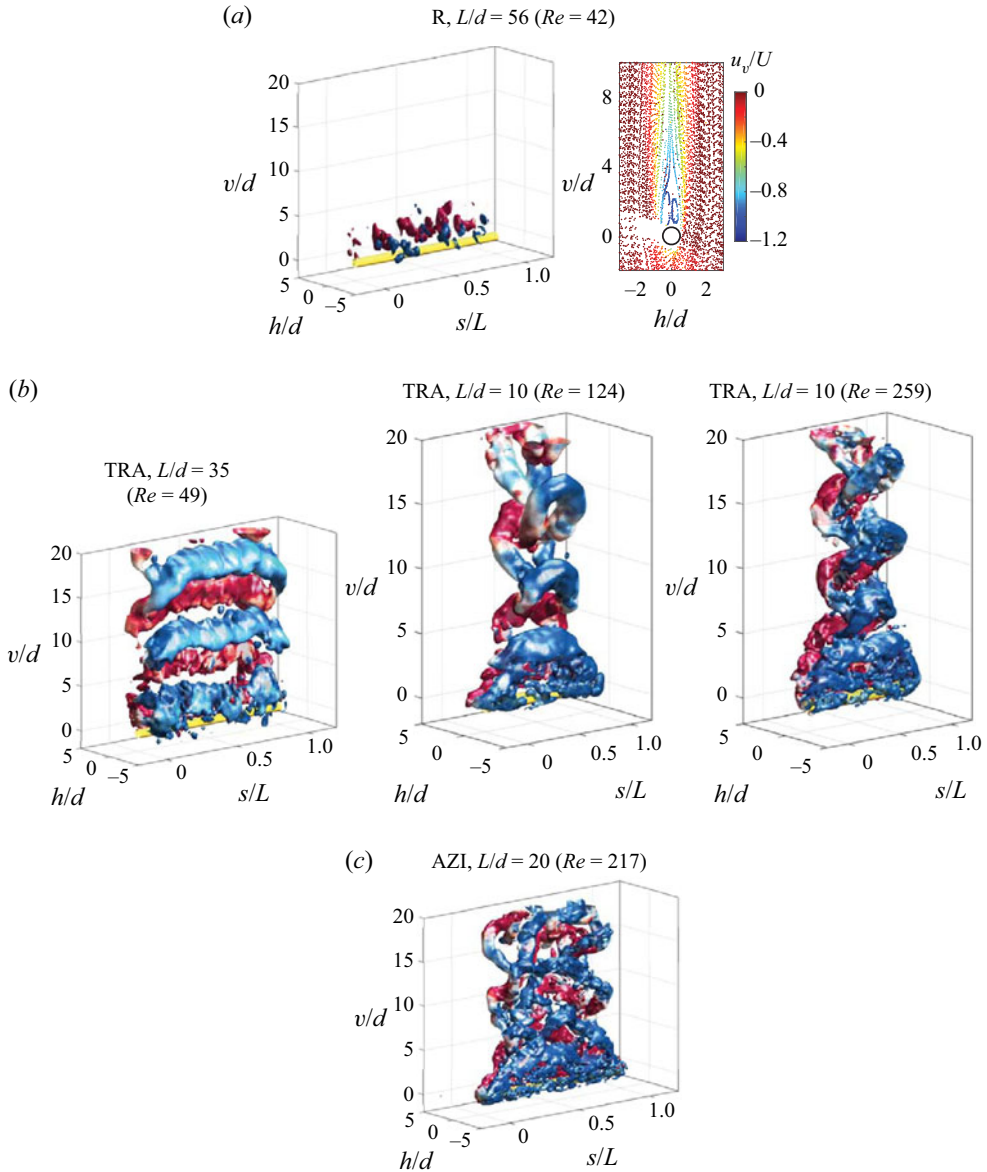
Figure 6. Wake patterns in the RBM regimes. (*a*) On the left, instantaneous iso-surfaces of the $\lambda_2$ criterion ($\lambda_2 d^2/U^2 = -0.001$) coloured by iso-contours of the spanwise vorticity ($\omega_s d/U \in [-0.1, 0.1]$, blue to red); on the right, particle trajectories coloured by the vertical velocity at $s \approx L/2$, in the R regime ($Ar \simeq 40$, $Re \simeq 42$, $Ca \simeq 15.5$, $L/d \simeq 56$); the cylinder surface is coloured yellow, and its contour is delimited by a black line in the plot on the right. (*b*) Same as the left-hand plot of (*a*) in the TRA regime ($d = 1.12$ mm, $Ar \simeq 47$, $Re \simeq 49$, $Ca \simeq 2.6$, $L/d \simeq 35$; $d = 1.9$ mm, $Ar \simeq 103$, $Re \simeq 124$, $Ca = O(10^{-2})$, $L/d \simeq 10$; $d = 2.7$ mm, $Ar \simeq 175$, $Re \simeq 259$, $Ca = O(10^{-5})$, $L/d \simeq 10$), with $\lambda_2 d^2/U^2 = -0.005$ in the cases depicted in the middle and right-hand panels. (*c*) Same as the left-hand plot of (*a*) in the AZI regime ($Ar \simeq 161$, $Re \simeq 217$, $Ca \sim 0$, $L/d \simeq 20$), with $\lambda_2 d^2/U^2 = -0.005$.

value in the last TRA case, visualized in figure 6(*b*). It can be noted that the irregular small-scale modulations of the vortical structures are analogous in both cases. A major difference with the TRA regime patterns, however, resides in the spanwise antisymmetry

**946** A16-16

of vorticity distribution close to the body. In the AZI regime, the shedding of a given vortex does not occur simultaneously on each side of the cylinder. Instead, the detachment of a positive spanwise vortex ($\omega_s > 0$) on one side appears to coincide with the detachment of a negative vortex ($\omega_s < 0$) on the other side. This aspect will be analysed in the following.

The above observations concerning the structural responses and global shape of the wake in the different RBM regimes suggest a close connection between body oscillations and flow unsteadiness. An attempt to clarify such a connection is proposed below.

### 4.3. *Flow–structure coupling*

The R regime is characterized by the absence of significant body oscillations and by a steady flow; it will not be investigated further.

In order to quantify flow unsteadiness in the TRA and AZI regimes, time series of the horizontal component of flow velocity are collected along a spanwise line located 5 diameters downstream of the body ($(v, h) = (5, 0)$). The frequency spectra of flow velocity fluctuations are plotted along the span in figure 7($a$–$c$), for selected cases (iso-contours). The spanwise modulations in velocity fluctuation intensity reflect the 3-D wake structures depicted in figure 6. In particular, fluctuation intensity tends to drop close to the body ends. A relatively constant level of fluctuation can be noted in the first TRA case (figure 7$a$), where the flow was found to be invariant (i.e. close to two-dimensional) over most of the span. In spite of the spanwise modulations in fluctuation magnitude, the dominant frequency of flow unsteadiness remains globally constant along the body length, in all cases. Flow unsteadiness frequency varies from one case to the other. Such variation is expected considering the different values of $Re$ and $L/d$, and the distinct dynamics of the body. For comparison purposes, the vortex shedding frequency reported by Williamson & Brown (1998) for a fixed cylinder in the absence of end effects is indicated by a black dashed line in each plot.

The span-averaged dominant frequency of cylinder horizontal oscillation is superimposed on flow velocity spectra in figure 7($a$–$c$) (plain blue lines). Body oscillation frequency and flow unsteadiness frequency are found to coincide at each spanwise location. Body motion and flow unsteadiness are thus synchronized, a condition generally referred to as lock-in in the context of vortex-induced vibrations of elastically mounted bodies (Williamson & Govardhan 2004). Flow–body synchronization is established in all studied cases of TRA and AZI regimes.

Synchronization mechanisms can be analysed further by comparing the spanwise evolutions of the phases associated with the dominant frequencies of body responses and flow velocity fluctuations. These phases are plotted in figure 7($d$–$f$), for each selected case; as in figure 5, the phases are centred about their span-averaged values. In the TRA regime, flow fluctuation phase remains close to constant over a wide region about the midspan point, as body response phase. This corroborates the above observation based on instantaneous visualizations, concerning the symmetry of vortical structure formation along the span, i.e. simultaneous shedding in the $s/L < 0.5$ and $s/L > 0.5$ regions. The phase opposition between each side of the cylinder, associated with the AZI regime responses, can also be noted in flow unsteadiness (even though defined less clearly). Such distribution of the phase confirms the above-mentioned antisymmetry of the wake dynamics (opposite sign vortices shed simultaneously on each side), which is thus found to match the antisymmetry of body rotary oscillation. Phase analysis shows that body motion and flow unsteadiness are not only temporally synchronized but also spatially locked to each other.
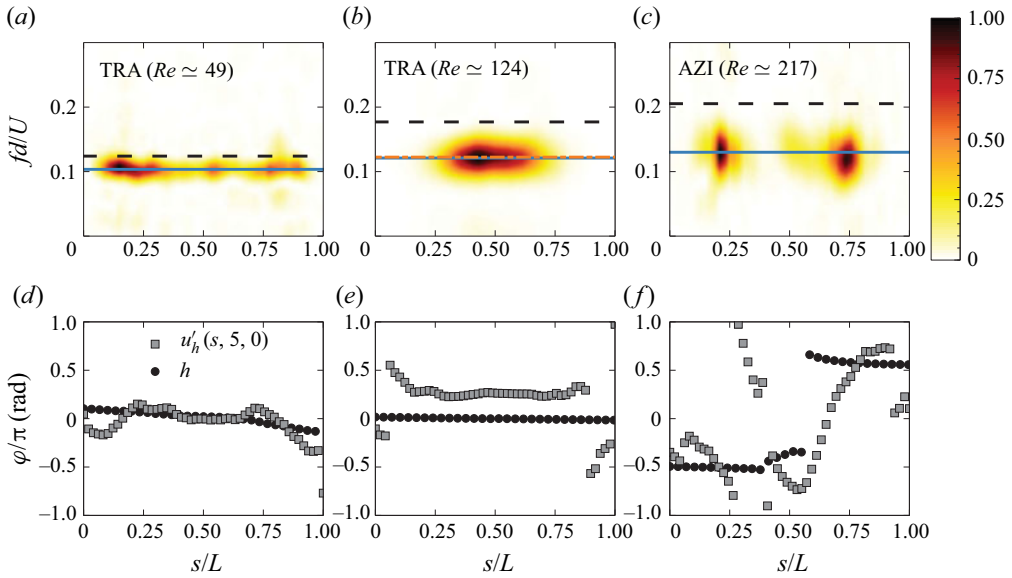
Figure 7. (*a,d,b,e*) Flow–structure synchronization in the TRA regime, with: (*a,d*) $d = 1.12$ mm, $Ar \simeq 47$, $Re \simeq 49$, $Ca \simeq 2.6$, $L/d \simeq 35$; and (*b,e*) $d = 1.9$ mm, $Ar \simeq 103$, $Re \simeq 124$, $Ca = O(10^{-2})$, $L/d \simeq 10$. (*c,f*) Flow–structure synchronization in the AZI regime ($Ar \simeq 161$, $Re \simeq 217$, $Ca = O(10^{-4})$, $L/d \simeq 20$). (*a–c*) Spanwise evolution of the frequency spectrum (PSD) of the horizontal component of flow velocity sampled 5 diameters downstream of the body. The spectrum amplitudes are normalized by the peak value. In each case, a plain blue line denotes the dominant oscillation frequency identified in figure 5, and a black dashed line indicates the vortex shedding frequency for a long stationary cylinder, $fd/U = 0.2731 - 1.1129/\sqrt{Re} + 0.4821/Re$ (Williamson & Brown 1998). In (*b*), an orange dashed-dotted line indicates the shedding frequency reported by Inoue & Sakuragi (2008) for an $L/d = 10$, stationary cylinder at $Re = 100$. (*d–f*) Spanwise evolution of the phases associated with the dominant frequencies of the horizontal component of flow velocity downstream of the body ($u'_h$) and of the horizontal oscillation; the phases are centred about their span-averaged values.

This spatio-temporal synchronization could explain the spanwise distribution of flow fluctuation intensity visualized in figure 7(*c*) for the AZI regime: intensity peaks appear close to $s/L = 0.21$ and $L/d = 0.73$, i.e. in regions of significant structural response amplitudes (but far enough from the body ends, where fluctuation intensity is low in all studied cases); the central region, where the rotary motion results in lower oscillation amplitudes, exhibits lower intensity fluctuations of flow velocity.

A complementary vision of flow–body synchronization in the TRA and AZI regimes is presented in figure 8, where phase-averaged (using between 3 and 4 cycles) iso-contours of the spanwise vorticity are plotted in selected planes perpendicular to the cylinder axis, for two typical cases. The selected planes correspond to the body ends and midspan point, as well as the regions where flow fluctuation intensity peaks in the AZI regime case (figure 7c). The phase-averaging process is based on body response. The phase depicted in figure 8 is chosen arbitrarily and corresponds to the phase of the cycle where body oscillation amplitude vanishes. The fact that vortex shedding is captured by the phase-averaging process suggests that it is synchronized with body motion.

At $s/L = 0.21$ and $L/d = 0.73$, the planar structure of the wake resembles the 2S pattern, with two counter-rotating vortices shed per oscillation cycle (Williamson & Govardhan 2004), regardless of the 3-D shape of the overall vortical structure (e.g. hairpin). A comparison of the vorticity fields at these spanwise locations shows that the

**946** A16-18
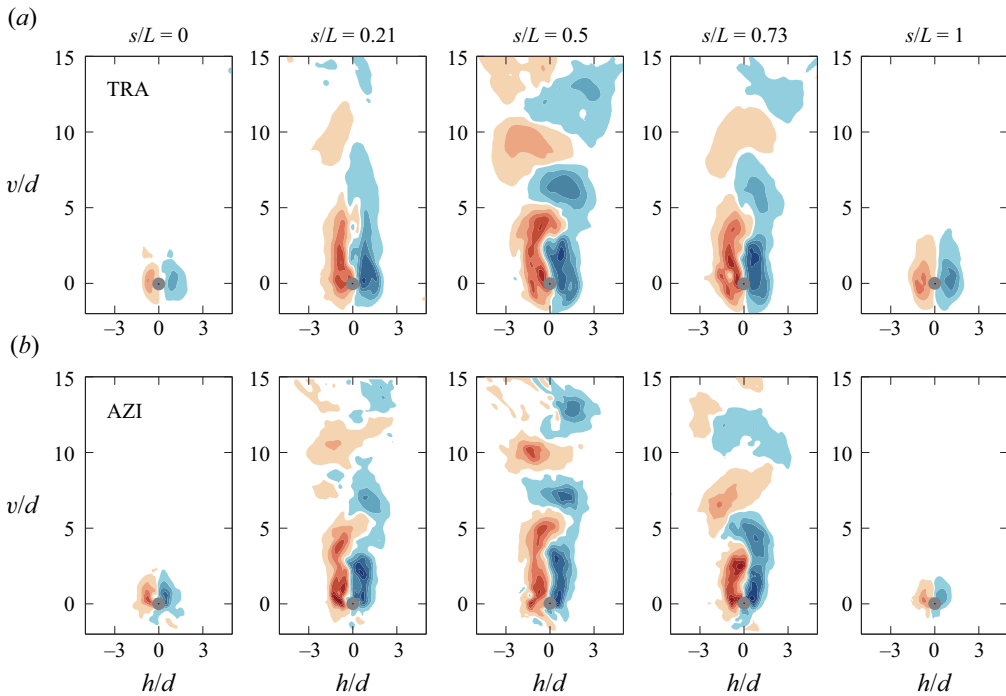
Figure 8. Phase-averaged vortex shedding process in (*a*) the TRA regime ($d = 1.9$ mm, $Ar \simeq 103$, $Re \simeq 124$, $Ca = O(10^{-2})$, $L/d \simeq 10$), and (*b*) the AZI regime ($d = 2.55$ mm, $Ar \simeq 161$, $Re \simeq 217$, $Ca = O(10^{-4})$, $L/d \simeq 20$). Phase-averaged iso-contours of the spanwise vorticity ($\omega_s d/U \in [-1, 1]$, blue to red) are plotted in selected planes perpendicular to the cylinder axis, $s/L \simeq 0, 0.21, 0.5, 0.73, 1$. The selected phase corresponds to the phase of the cycle where the amplitude of oscillation vanishes. In each plot, a horizontal segment (barely visible) denotes the cylinder trajectory.

alternately shed vortices are in phase in the TRA regime and in phase opposition in the AZI regime, thus matching body response phasing. As also observed in the instantaneous visualizations in figure 6, the alternating vortex shedding ceases in the cylinder end regions. At the midspan point, in the AZI regime, the alternating shedding is expected to be replaced by the simultaneous shedding of opposite sign vortices, as reported previously near vibration nodes for flexible cylinders (e.g. figure 12 in Newman & Karniadakis 1997). Such a pattern is not observed in the present case where the phase opposition between vortex formation on each side of the body is accommodated by a global asymmetrical wake structure, as discussed in the following; such an asymmetrical structure differs from the strictly antisymmetrical structure reported by Newman & Karniadakis (1997).

To visualize further the wake dynamics associated with the AZI regime, instantaneous iso-surfaces of the $\lambda_2$ criterion coloured by iso-contours of spanwise vorticity are plotted in figure 9, at five selected instants over one oscillation cycle. The different instants are indicated in figure 9(*a*), which represents selected time series of cylinder horizontal displacement at $s = 0$ and $s = L$, i.e. body ends. Based on these visualizations and on the phasing identified in figure 7($f$), the following scenario can be proposed to describe wake dynamics. Each vortex starts to detach from the cylinder in the central region. As it is convected downstream, the vortex is progressively peeling off from the body, towards its ends. This process is comparable to the hairpin vortex formation observed in the TRA regime (figure 6*b*). However, in the AZI regime, the propagation of the detachment points

of the vortex, from the central region towards each end, is not strictly symmetrical for $s/L < 0.5$ and $s/L > 0.5$, so that the vortex detaches from one end while it is still attached to the body at the other end. Such a time difference in vortex detachment can be visualized at instant A (figure 9b): the blue vortex that is close to be shed but still attached near the left end (green arrow) has already been shed on the right side of the body (orange arrow). As a result, the bent vortices observed in the wake are not symmetrical about the midspan point, and they appear to be slightly inclined in the $(s, v)$ plane. A comparable asymmetry/inclination can be noted in the dye visualization reported by Toupoint *et al.* (2019) (figure 17c in that paper). The above described process repeats successively for the positive and negative vortices, so that positive and negative vortices are formed and then shed simultaneously from each side of the cylinder, leading to the phase opposition mentioned previously. At instant A in the flow visualization of figure 9(*b–f*), a red vortex is close to be shed near the right end of the body (black arrow), simultaneously with the blue vortex indicated by a green arrow near the left end.

To summarize, the R regime where no significant structural responses emerge is associated with a steady flow. The typical translatory and rotary responses of the TRA and AZI regimes are restricted essentially to the horizontal plane; they are close to periodic and exhibit limited amplitudes, of the order of 0.03 body diameters. Both regimes involve a condition of spatio-temporal synchronization between body oscillations and flow unsteadiness. The TRA regime may develop under a variety of flow patterns, globally symmetrical about the midspan point, and ranging from spanwise-invariant vortex rows to hairpin vortex shedding. These patterns are all associated with a phase of flow velocity fluctuations that remains constant along a portion of the span about the midspan point, as body response phase. In contrast, the AZI regime is accompanied by an asymmetrical shedding pattern that results in an antisymmetrical distribution of spanwise vorticity and a phase opposition between flow velocity fluctuations on each side of the body, which matches the body behaviour phasing.

## 5. Bending oscillation regimes

In addition to the rigid-body responses described in § 4, freely falling cylinders may also exhibit bending oscillations (BO) in some regions of the $(Ar, L/d, Ca)$ parameter space. Such BO regimes have been identified in a prior study that was based on structural response measurements only (Ern *et al.* 2020). This previous work showed that BO regimes may involve different vibration patterns that are close to the structural modes of an unsupported beam. The successive regimes were termed accordingly, based on the horizontal responses: $M_i$ designates the regime involving the $i$th mode. Two cases, representative of the $M_1$ and $M_2$ regimes, have been selected (table 1) and are examined in the following. The description of the body behaviour reported in the above-mentioned study is complemented in § 5.1. Then the typical patterns of the flow and its interaction with flexible body motion are explored in § 5.2 and § 5.3, respectively.

### 5.1. *Structural responses*

The bending oscillations of the cylinder in the selected cases of the $M_1$ and $M_2$ regimes are quantified in figure 10. Supplementary movie 4 depicts the cylinder oscillations during its fall under the $M_1$ regime.

The fact that the successive minima of the horizontal response envelopes (figure 10a,c) are close to zero amplitude indicates that the structural oscillations occurring in this
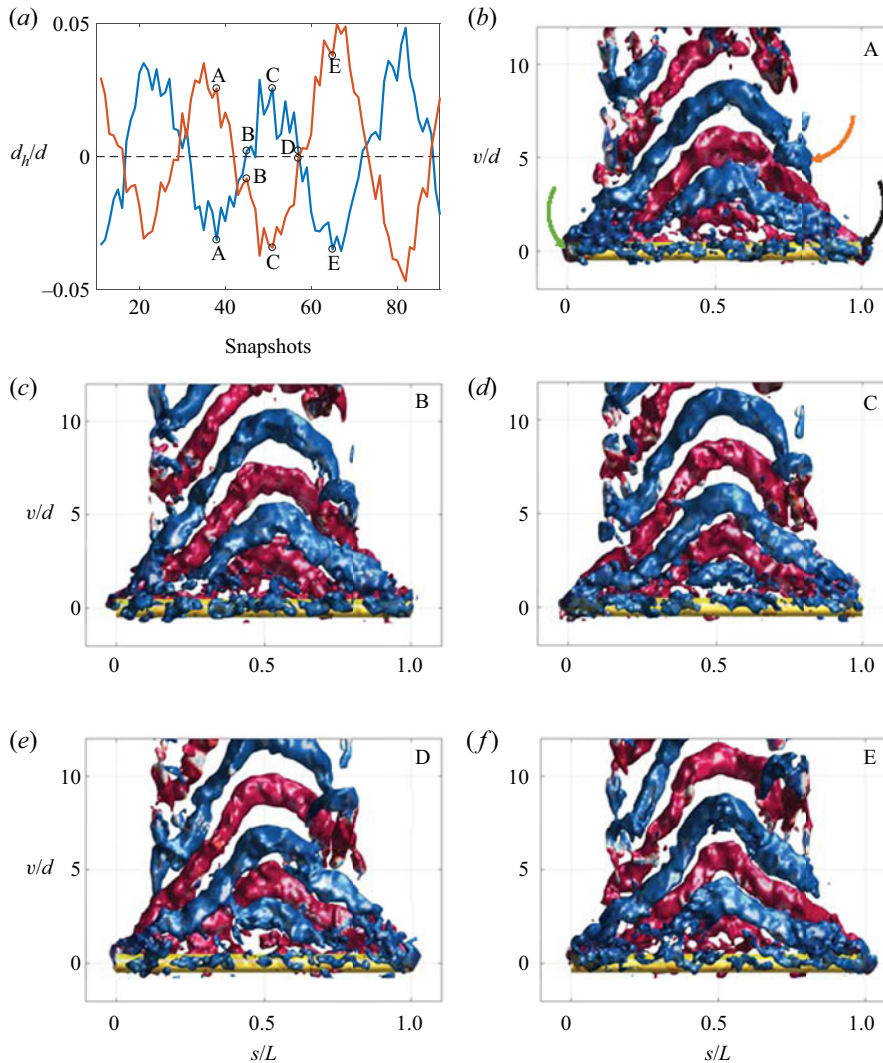
Figure 9. Wake dynamics in the AZI regime ($d = 2.55$ mm, $Ar \simeq 161$, $Re \simeq 217$, $Ca = O(10^{-4})$, $L/d \simeq 20$). (*a*) Time series of cylinder horizontal displacement at $s = 0$ (blue) and $s = L$ (orange). (*b–f*) Instantaneous iso-surfaces of the $\lambda_2$ criterion ($\lambda_2 d^2/U^2 = -0.03$) coloured by iso-contours of spanwise vorticity ($\omega_s d/U \in [-0.1, 0.1]$, blue to red), at the five selected instants indicated in (*a*).

direction consist mainly of standing waves. The succession of nodes and crests reflects the shape of the structural mode involved in each case: the first mode with two nodes, and the second mode with three nodes. Vertical response amplitudes exhibit tangible spanwise modulations that betray the presence of bending oscillations also in this direction. However, no clear topology of response shapes can be established, and no dominant structural mode emerges. As in the RBM regimes, the horizontal responses are much larger than the vertical ones, and the body appears to oscillate essentially in the horizontal plane. It should, however, be mentioned that the responses encountered in the BO regimes, typically close to 0.3 and 0.02 diameters in the horizontal and vertical directions, respectively, are one order of magnitude larger than those observed in the RBM regimes.
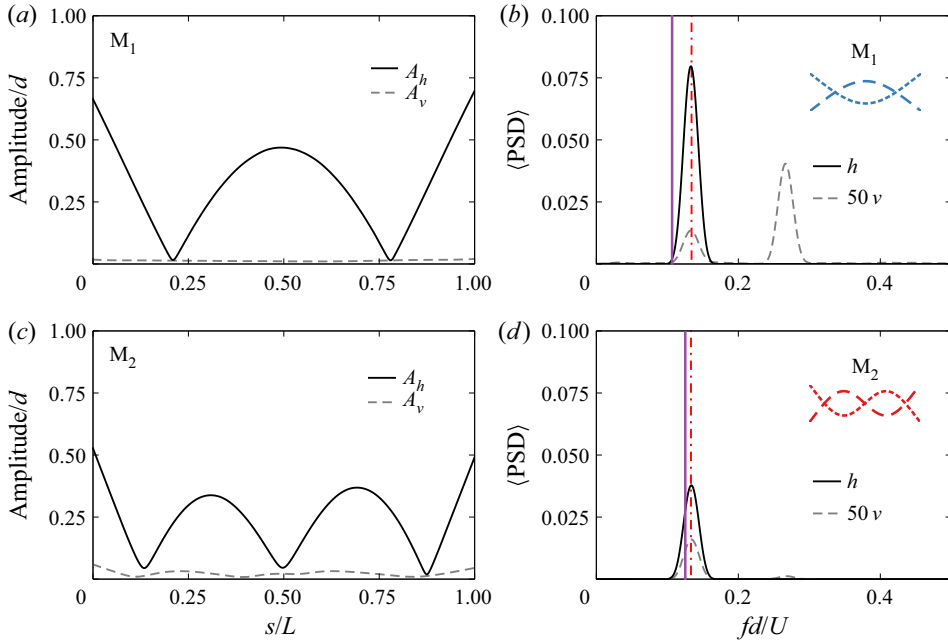
Figure 10. Structural responses in the BO regimes. (*a,c*) Spanwise evolution of the time-averaged amplitude of oscillation and (*b,d*) span-averaged frequency spectrum (PSD) of the oscillation, in the horizontal (plain line) and vertical (dashed line) directions, in (*a,b*) the $M_1$ regime ($Ar \simeq 45$, $Re \simeq 42$, $Ca \sim 36$, $L/d \simeq 68$) and (*c,d*) the $M_2$ regime ($Ar \simeq 40$, $Re \simeq 37$, $Ca \sim 210$, $L/d \simeq 107$). In (*b,d*), the oscillation frequencies reported in Ern *et al.* (2020) based on shadowgraphy experiments, for the same cylinders, are indicated by red dashed-dotted lines, and the natural frequencies of the first and second structural modes, computed as $f_i = \alpha_i d/L^2 \sqrt{E/(\rho_c + \rho_f)}$, with $\alpha_1 \approx 0.890$ and $\alpha_2 \approx 2.454$, respectively, are denoted by purple lines.

These BO amplitudes are comparable to those usually reported for elastically mounted rigid cylinders and pinned flexible cylinders subjected to vortex-induced vibrations at similar *Re* values (e.g. Mittal & Singh 2005; Bourguet 2020).

The span-averaged spectra of the horizontal and vertical oscillations are plotted in figure 10(*b,d*). In both directions, the responses are close to periodic. The horizontal oscillations are dominated by a single frequency, as in the RBM regimes. This frequency, close to $fd/U = 0.13$ in each case, coincides with that issued from shadowgraphy measurements (Ern *et al.* 2020), shown with red dashed-dotted lines in figure 10(*b,d*). It may deviate from the natural frequency of the corresponding structural mode ($f_1 d/U = 0.107$ in the first case, and $f_2 d/U = 0.126$ in the second case, where the added mass coefficient is estimated by its potential flow value of 1; purple solid lines in the plots).

Such a departure from the natural frequency is a typical phenomenon, often associated with the lock-in mechanism, especially at low mass ratios (Williamson & Govardhan 2004; Bourguet *et al.* 2011*a*). This aspect will be addressed in § 5.3. Due to the (theoretical) symmetry of the physical system and the ratio of 2 between the streamwise and transverse fluid forcing for a rigidly mounted circular cylinder, the vertical oscillations are expected to occur at twice the horizontal response frequency. These components indeed appear in response spectra (figure 10*b,d*), but they are accompanied by first harmonic contributions, which actually dominate the response spectrum in the $M_2$ regime case. The combination of first and second harmonic contributions to streamwise structural dynamics is observed frequently for supported flexible cylinders subjected to
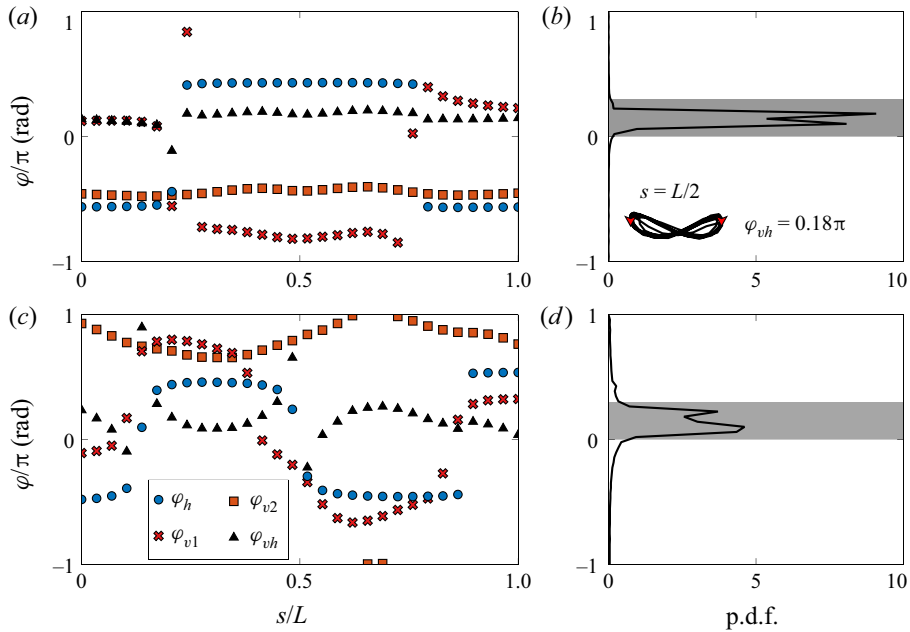
**946** A16-22

Figure 11. Phasing of the structural responses in ($a,b$) the $M_1$ regime ($Ar \simeq 45$, $Re \simeq 42$, $Ca \sim 36$, $L/d \simeq 68$), and ($c,d$) the $M_2$ regime ($Ar \simeq 40$, $Re \simeq 37$, $Ca \sim 210$, $L/d \simeq 107$). ($a,c$) Spanwise evolution of the phases associated with the dominant frequency of the horizontal oscillation ($\varphi_h$) and the first and second harmonics of the vertical oscillation ($\varphi_{v1}$, $\varphi_{v2}$), as well as the phase difference $\varphi_{vh} = \varphi_{v2} - 2\varphi_h$. ($b,d$) Probability density function (p.d.f.) of the phase difference $\varphi_{vh}$ between the horizontal and vertical responses; shaded areas indicate the dominant phase difference range reported in Bourguet (2020) for pinned flexible cylinders. In ($b$), the inset represents the horizontal versus second harmonic vertical responses (i.e. filtered orbit) at $s = L/2$ in the $M_1$ regime ($\varphi_{vh} = 0.18$).

vortex-induced vibrations (Huera-Huarte & Bearman 2009; Seyed-Aghazadeh, Edraki & Modarres-Sadeghi 2019); this may be attributed to slight asymmetries in the experimental configuration (e.g. small permanent deformation, not strictly circular cross-section, etc.) but also to spontaneous symmetry breaking in the system response, due for instance to the incompatibility between the fluid forcing frequency and the shape of the corresponding mode (Gedikli, Chelidze & Dahl 2018), as well as the possible emergence of asymmetrical vortex shedding patterns (Singh & Mittal 2005).

The phases associated with the dominant frequencies of the horizontal and vertical responses are represented along the span in figure 11($a,c$), for the selected cases. In each case, the phase of the horizontal response ($\varphi_h$) is a constant piecewise function of $s$, with $\pi$ jumps at the nodes. Such a phase distribution confirms the standing wave nature of the oscillation. In the vertical direction, the phases associated with the first ($\varphi_{v1}$) and second ($\varphi_{v2}$) harmonics exhibit less clearly defined evolutions. The first harmonic components appear to be mixtures of standing and travelling wave patterns, while the phases of the second harmonic components remain relatively constant along the span; in both cases, the second harmonic contribution could thus be regarded as an RBM, modulated slightly along the span.

The phasing of the horizontal and vertical responses determines, at each spanwise location, the shape of cylinder trajectory. Previous studies concerning vortex-induced vibrations of rigid and flexible cylinders have shown that trajectory shape is linked closely to flow–structure energy transfer (i.e. excitation/damping of the structure by the

flow) and that some shapes are more likely to occur under lock-in (Dahl *et al.* 2010; Bourguet *et al.* 2011*b*; Fan *et al.* 2019). For a frequency ratio of 1 between the vertical and horizontal responses, the cylinder exhibits elliptical trajectories, while it describes figure-eight orbits when the frequency ratio is equal to 2. In the present cases, where both first and second harmonic contributions arise in the vertical response spectra, the trajectory is a figure-eight with unequal loop sizes. In a recent work concerning pinned flexible cylinders at comparable *Re*, a dominant trajectory shape was identified over wide ranges of body aspect ratios and excited modes (Bourguet 2020). This dominant trajectory consists of a figure-eight shape, close to a crescent bent downstream (i.e. upwards), where the body moves upstream when reaching transverse oscillation maxima; such an orbit orientation was referred to as counter-clockwise in prior studies (Dahl *et al.* 2010).

For comparison purposes with this persistent phasing mechanism, focus is placed here on the phase difference between the horizontal response and the second harmonic of the vertical response, $\varphi_{vh} = \varphi_{v2} - 2\varphi_h$. For each selected case, this phase difference is computed at each spanwise location (figure 11*a*,*c*), and the corresponding probability density functions (p.d.f.) are plotted in figure 11(*b*,*d*). In each case, the phase difference is found to be restricted to a narrow range, and it can be observed that this range coincides closely with that identified in Bourguet (2020) (shaded areas in the plots). The typical, dominant trajectory of the body is visualized in the inset of figure 11(*b*) at the midspan point, in the $M_1$ regime case. It is recalled that the vertical oscillations examined here exhibit low amplitudes and involve both first and second harmonic contributions. However, the present results confirm previous observations and suggest that the phasing mechanism of the horizontal and vertical responses could be a generic feature for flexible cylinders subjected to bending oscillations in this *Re* range, regardless of the supported or unsupported end conditions and the structural modes at play.

### 5.2. *Flow patterns*

The cases of $M_1$ and $M_2$ regimes examined here are characterized by low Reynolds number values, $Re = 42$ and $Re = 37$, respectively. For a rigidly mounted cylinder and in the absence of end effects, the flow is expected to be steady in this *Re* range (Williamson 1996). However, prior works have shown that when one or more degrees of freedom are added to the structure, the flow may become unsteady at much lower *Re* than the critical value of 47, typically down to $Re \approx 20$ depending on $m^*$. Such a phenomenon was reported for rigid cylinders (Cossu & Morino 2000; Mittal & Singh 2005; Meliga & Chomaz 2011; Dolci & Carmo 2019; Boersma *et al.* 2021), as well as pinned flexible cylinders (Bourguet 2020); it was also conjectured to occur for freely falling flexible cylinders in Ern *et al.* (2020), based on bending oscillations measurements only. The present measurements confirm that the flows associated with the selected cases of BO regimes are unsteady, despite the low *Re* values.

The typical wake patterns encountered downstream of the oscillating cylinder in the $M_1$ and $M_2$ regimes are visualized in figure 12 via instantaneous iso-surfaces of the $\lambda_2$ criterion, coloured by iso-contours of the spanwise vorticity, as in figure 6. Illustrations including wake and cylinder dynamics for the two BO regimes are available in supplementary movies 5 and 6. A first overview of these visualizations indicates that wake patterns are composed mainly of regularly shed, spanwise vortex rows globally parallel to the cylinder axis. These vortex rows and their connections close to the body ends resemble those depicted in figure 6(*b*) in the TRA regime, for $L/d = 35$. A closer examination, however, reveals some subtle differences. Two elements can be noted.
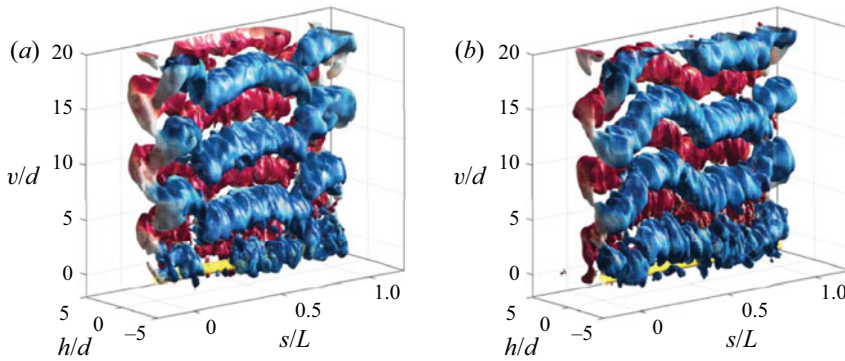
Figure 12. Wake patterns in the BO regimes. Instantaneous iso-surfaces of the $\lambda_2$ criterion ($\lambda_2 d^2/U^2 = -0.001$) coloured by iso-contours of the spanwise vorticity ($\omega_s d/U \in [-0.1, 0.1]$, blue to red) for (*a*) the M$_1$ regime ($Ar \simeq 45$, $Re \simeq 42$, $Ca \sim 36$, $L/d \simeq 68$), and (*b*) the M$_2$ regime ($Ar \simeq 40$, $Re \simeq 37$, $Ca \sim 210$, $L/d \simeq 107$).

First, slight distortions of the successive vortex rows appear at specific spanwise locations, which seem to coincide with the nodes of the horizontal structural responses. Second, on each side of these distortion points, positive vortex rows are found to be roughly aligned with negative vortex rows, i.e. a phase shift close to $\pi$ occurs in the wake at these locations as observed previously for the AZI mode. These elements as well as the value of the body oscillation frequency, close to the vortex shedding frequency reported at comparable *Re* by Buffoni (2003), indicate a link between body motion and flow unsteadiness, as in the RBM regimes and as also hypothesized in Ern *et al.* (2020).

### 5.3. *Flow–structure coupling*

The procedure introduced in § 4.3 to clarify the connection between solid behaviour and flow unsteadiness in the RBM regimes is applied here to the selected M$_1$ and M$_2$ regime cases. For each case, the frequency spectra of the horizontal flow velocity fluctuations, collected 5 diameters downstream of the cylinder, are plotted along the span in figure 13(*a*,*b*), together with the horizontal deformation frequency (plain blue line).

The spectral amplitudes of flow velocity fluctuations exhibit large spanwise modulations, but their dominant frequency remains constant and matches the structural oscillation frequency throughout the body length. In each case, this temporal synchronization occurs at a frequency that departs slightly from the structure natural frequency ($f_1$ or $f_2$, plain purple line). A slight deviation from the vortex shedding frequency identified by Buffoni (2003) (black dashed line) can also be noted.

The phases associated with the horizontal oscillation and flow fluctuation frequencies are plotted in figure 13(*c*,*d*). The phases are centred about their span-averaged values; the fact that the relative phase at $s = 0$ is the same in $M_2$ and different in $M_1$ is related to the chosen wake position. Phase comparison shows that a phase jump occurs in the flow at each node of the structural response. More precisely, it indicates that flow velocity fluctuations are in phase opposition on each side of the nodes, which confirms the above-mentioned phase opposition in vortex distribution along the span, i.e. the successive alignment of negative and positive vortices on each side of the nodes. As also observed in the RBM regimes, the intensity of flow unsteadiness tends to drop near the body ends. Away from the ends, flow unsteadiness intensity is found to follow the local amplitude of
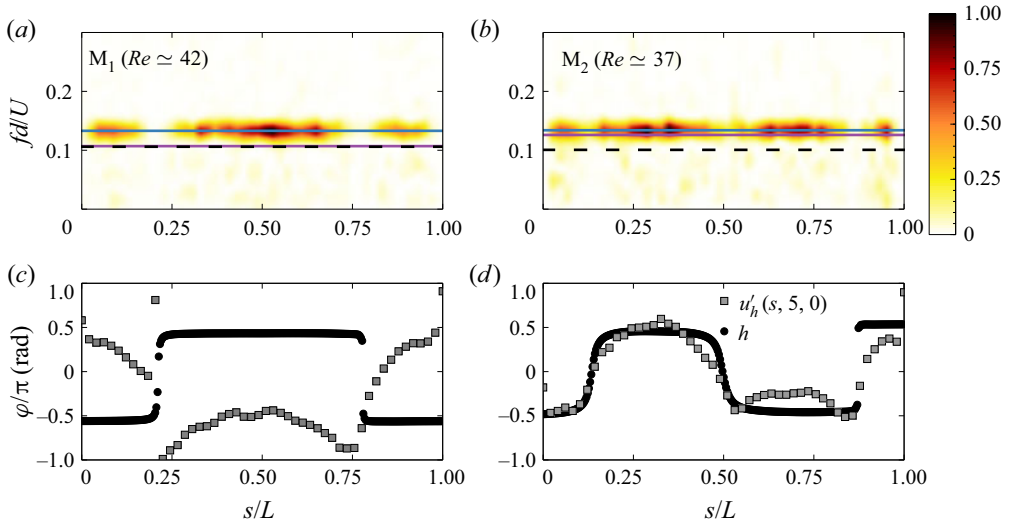
Figure 13. Same as figure 7 in (*a,c*) the $M_1$ regime ($Ar \simeq 45$, $Re \simeq 42$, $Ca \sim 36$, $L/d \simeq 68$), and (*b,d*) the $M_2$ regime ($Ar \simeq 40$, $Re \simeq 37$, $Ca \sim 210$, $L/d \simeq 107$). The natural frequencies of the first and second structural modes are denoted by plain purple lines in (*a,c*) and (*b,d*), respectively. The vortex shedding frequencies reported by Buffoni (2003) at subcritical *Re*, for rigid circular cylinders, are indicated by black dashed lines.

the structural response. In particular, minima and maxima of flow velocity fluctuations are observed near the nodes and antinodes of the horizontal response, respectively.

Therefore, body motion and flow unsteadiness are both temporally and spatially locked, as in the RBM regimes. This spatio-temporal lock-in mechanism involving bending oscillations of the body was described previously at comparable *Re*, for pinned cylinders (Bourguet 2020). The present results show that such a synchronization mechanism may also occur for unsupported, freely falling cylinders.

The spatio-temporal lock-in mechanism is accompanied by a cellular structure of the wake where each cell is delimited by the horizontal deformation nodes. A visualization of these patterns is presented in figure 14 via phase-averaged iso-surfaces of spanwise vorticity. As in figure 8, the phase-averaging process is based on the horizontal response of the body (using between 7 and 8 cycles), and the selected phase corresponds to the phase of the cycle where the response vanishes. In the $(s, v)$ and $(h, s)$ plane visualizations (figure 14), the spanwise locations of the horizontal response nodes are indicated by green dashed lines. Complementary side views show the interconnections of the successive vortex rows in the cylinder end region (figure 14, lateral views). Figure 14 can be examined together with figure 15, which represents iso-contours of the phase-averaged spanwise vorticity field in selected planes along the span. The planes are located at the body end and at horizontal vibration nodes and antinodes, over half of the span. The selected phases correspond to maximum and minimum amplitudes of horizontal oscillation, as indicated by cylinder position in each plot.

The 3-D visualizations in figure 14 (frontal views) show evidence of the local distortions of the spanwise vortices near response nodes, as well as their relatively spanwise-invariant shape in-between. Within each cell, i.e. between two successive nodes, figure 15 shows that two counter-rotating vortices form per oscillation cycle (2S pattern; Williamson & Govardhan 2004). The phase of flow velocity fluctuations may exhibit some variations in each cell (figure 13*c,d*) which is reflected in the wake by a slight streamwise bending
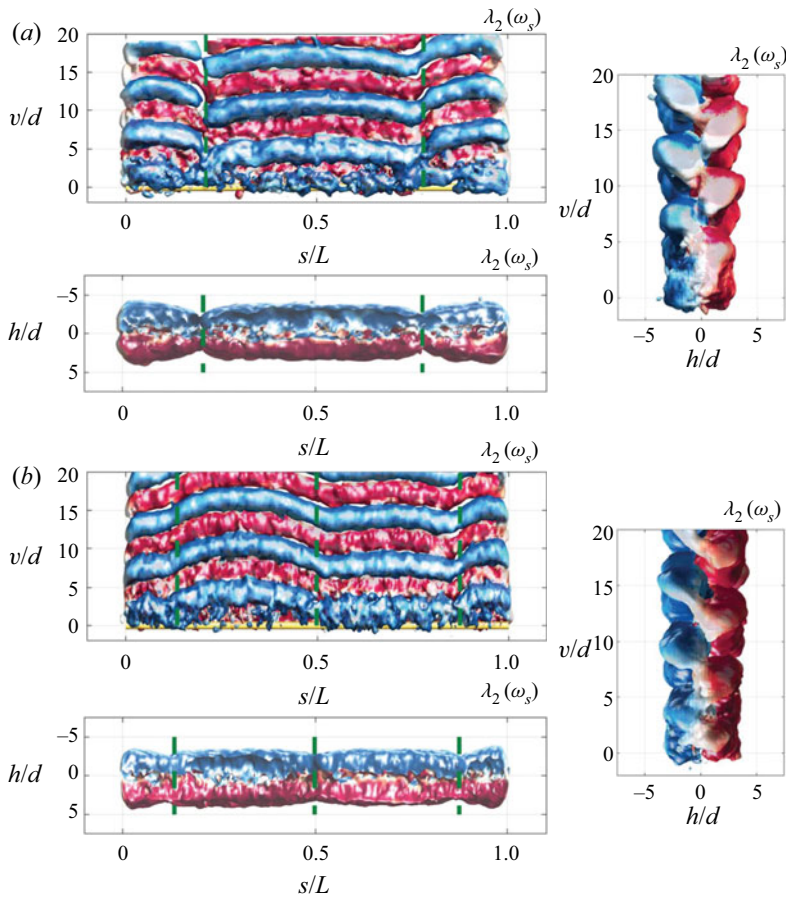
Figure 14. Phase-averaged flow patterns in (*a*) the $M_1$ regime ($Ar \simeq 45$, $Re \simeq 42$, $Ca \sim 36$, $L/d \simeq 68$), and (*b*) the $M_2$ regime ($Ar \simeq 40$, $Re \simeq 37$, $Ca \sim 210$, $L/d \simeq 107$). Frontal, vertical (at $v/d \simeq 5$) and lateral views of the phase-averaged iso-surfaces of the $\lambda_2$ criterion ($\lambda_2 d^2/U^2 = -8 \times 10^{-4}$) are shown, coloured by iso-contours of the spanwise vorticity ($\omega_s \in [-0.08, 0.08]$, blue to red). The selected phase corresponds to the phase of the oscillation cycle where the horizontal response vanishes. In frontal and vertical views, the spanwise locations of the horizontal response nodes are indicated by green dashed lines.

of the vortical structures (e.g. for $s/L \in [0.2, 0.5]$ in the $M_2$ regime case). On each side of a node, a positive vortex is found to coincide with a negative vortex, as mentioned previously. This global phase opposition is confirmed by the antisymmetrical structures of the vorticity fields represented in figure 15. The alignment of the adjacent vortex rows is, however, not perfect, as expected from the phase plots in figure 13(*c,d*): the phase jumps of the wake at the nodes are generally not strictly equal to $\pi$, contrary to those observed for the body responses. Another asymmetry can be noted, in the interconnection between the same-sign vortex rows. For comparable cellular patterns, prior works showed that each vortex row is connected, across the node region, to the previous and next vortex rows (e.g. figure 4 in Bourguet 2020). Here, generally, a single connection is observed, either with the previous or with the next adjacent vortex. This symmetry breaking in vortex connection is associated with the absence of symmetrical shedding patterns near the nodes, as those visualized by Newman & Karniadakis (1997); as a result, even in the node regions, wake shape resembles the 2S pattern (see figure 15, for instance). The above-mentioned
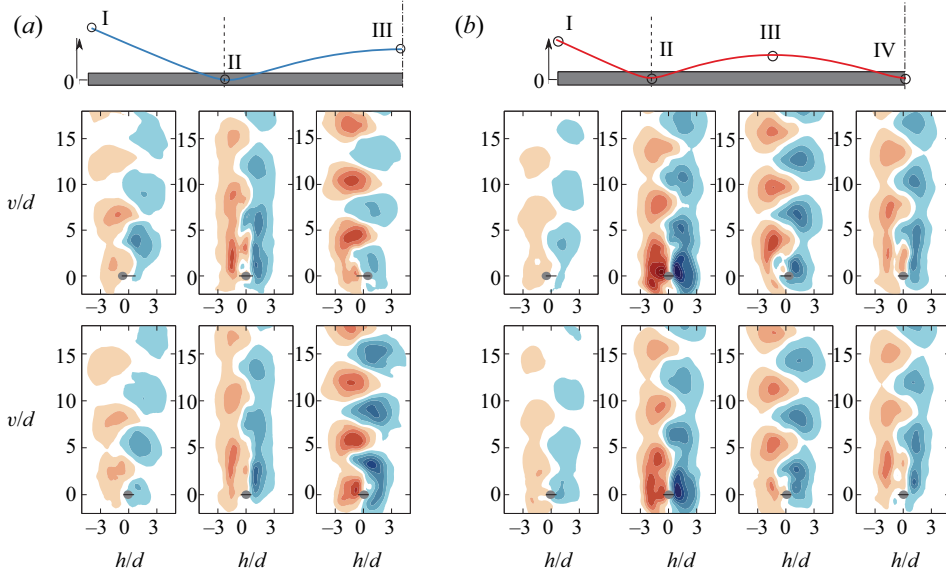
Figure 15. Same as figure 8 in (*a*) the M$_1$ regime ($Ar \simeq 45$, $Re \simeq 42$, $Ca \sim 36$, $L/d \simeq 68$), and (*b*) the M$_2$ regime ($Ar \simeq 40$, $Re \simeq 37$, $Ca \sim 210$, $L/d \simeq 107$), with $\omega_s d/U \in [-0.3, 0.3]$. For each case, the selected planes are indicated in a sketch (top) which represents the amplitude of the horizontal oscillation, over half of the cylinder span.

misalignment of vortex rows and asymmetries might be attributed to imperfections of the experimental configuration (e.g. small static deformation of the cylinder, slight inclination of the body as it falls, etc.). These asymmetries, however, have a limited impact on the overall structure of the cellular wake patterns encountered in the M$_1$ and M$_2$ regimes, which remain close to those associated with the occurrence of standing wave responses under lock-in, for pinned flexible cylinders (Bourguet 2020).

Previous studies concerning cylinders subjected to forced oscillations have emphasized the influence of oscillation properties (amplitude, frequency) on the shape of the recirculation region appearing in the near wake (e.g. Ramberg & Griffin 1974). The length of the recirculation region is particularly significant as it is related directly to the local drag force (Roshko 1993). Based on flow visualizations comparable to that presented in figure 6(*a*), the recirculation length, $L_r$, is measured at each spanwise location, as the streamwise distance between the cylinder surface and the point where $|u_v| > U$, i.e. the relative time-averaged (§ 3.2) vertical flow velocity with respect to the body changes sign. The spanwise distribution of $L_r$ is plotted in figure 16(*c*) for the M$_1$ and M$_2$ regimes. In spite of the dispersion inherent in the measurement technique (lack of seeding particles inside the recirculation region), a trend can be identified: the recirculation length tends to increase near the structural response nodes (vertical dashed lines) and to decrease in larger-amplitude response regions. To clarify this phenomenon, the recirculation lengths measured in both cases are plotted as functions of the local oscillation amplitude in figure 16(*c*). A global decrease of $L_r$ is noted as oscillation amplitude increases; a similar trend was reported by Ramberg & Griffin (1974) under forced vibrations. The size of the recirculation region is thus modulated along the span, and its modulation coincides locally with the deformation amplitude. This observation sheds light on another aspect of the close connection between body oscillation and wake structure. Due to the low amplitudes of the responses and the dispersion of $L_r$ values, it was not possible to establish clearly
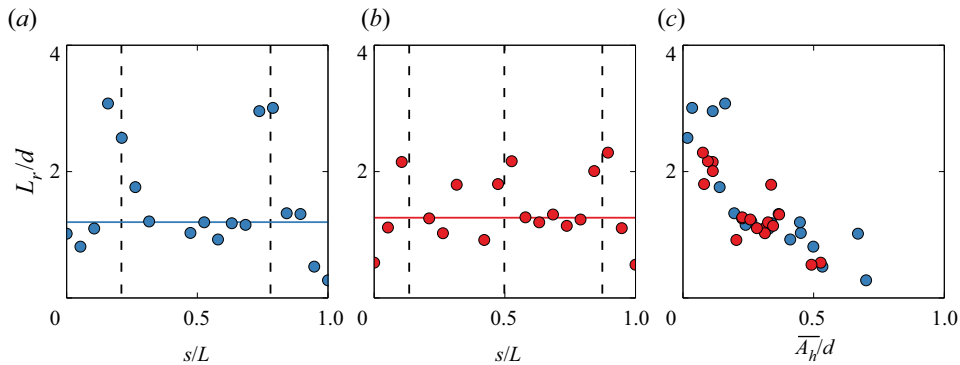
**946** A16-28

Figure 16. Evolution of the recirculation length, (*a,b*) along the span, and (*c*) as a function of the horizontal oscillation amplitude, in the $M_1$ regime ($Ar \simeq 45$, $Re \simeq 42$, $Ca \sim 36$, $L/d \simeq 68$, blue) and the $M_2$ regime ($Ar \simeq 40$, $Re \simeq 37$, $Ca \sim 210$, $L/d \simeq 107$, red). In (*a,b*), the locations of the horizontal response nodes are indicated by black dashed lines, and plain lines denote the span-averaged value of the recirculation length.

a comparable behaviour for the RBM regimes, even though it is likely to persist in these regimes, as suggested by the low-amplitude results in the above-mentioned study.

The principal features of the BO regimes examined in this section can be summarized as follows. As in the RBM regimes, body oscillations are close to periodic and occur essentially in the horizontal plane; yet their amplitudes are one order of magnitude larger, typically close to 0.3 and 0.02 diameters in the horizontal and vertical directions, respectively. The horizontal and vertical responses exhibit a specific phasing that matches that identified previously for pinned flexible cylinders. As also observed in the RBM regimes, the structural responses develop under a condition of spatio-temporal synchronization between the moving body and the flow, which is found to be unsteady, even though the Reynolds number is subcritical. The synchronization of the spanwise structure of the flow with the horizontal, standing wave responses of the body is accompanied by the formation of cellular patterns in the wake. Each cell consists of alternately shed spanwise vortex rows, globally aligned with the cylinder. The adjacent vortex rows are interconnected in response node regions where the phase shift of flow velocity fluctuations and antisymmetrical vorticity distribution coincide with response phase opposition. The close relation between body motion and wake organization is illustrated further by the joint evolution of the local amplitude of the body response and recirculation length.

## 6. Conclusions

The fluid–structure interaction problem corresponding to a flexible circular cylinder falling under the effect of buoyancy in a liquid otherwise at rest was investigated experimentally. Cylinders having different diameters and lengths were considered in order to explore different types of behaviour of the coupled fluid–body system. With the purpose of capturing simultaneously both solid and fluid dynamics, and to investigate their interaction, time-resolved tracking in three dimensions of body and fluid motions was performed in a large volume of measure, via DaVis software. The three-dimensional PTV method employed the Shake-The-Box algorithm to characterize the fluid motion about the cylinder by analysing trajectories of seeding fluorescent particles, and tomographic

reconstruction of the cylinder was performed from the same image sets to determine the associated body behaviour.

The paths considered feature either periodic rigid-body motions (RBM) of weak amplitude in translation or rotation, or periodic large-amplitude bending oscillations (BO). The results reported complement previous observations concerning these body motions and uncover the vortical flow structures associated with them, revealing their spatio-temporal synchronization. Oscillatory motions take over the R regime, a rectilinear vertical fall with the symmetry axis of the body lying horizontally, characterized by the absence of significant path or shape oscillations and a steady wake.

The TRA regime corresponds to a vertical fall with a rigid-body oscillation of the cylinder in a plane perpendicular to its symmetry axis. The associated wake is unsteady and composed of well-defined vortical structures shed downstream of the body. For a cylinder of aspect ratio $L/d = 35$, the counter-rotating vortices are parallel to the body axis, bending only near the body ends, where they connect to the adjacent vortex rows. As the cylinder aspect ratio is reduced, the vortices evolve towards hairpin structures. The AZI regime features an azimuthal oscillation of the cylinder axis in a horizontal plane, the body revolving now around its gravity centre with the ends moving in opposite directions. The associated unsteady wake is composed mainly of curved, asymmetrical spanwise vortices, presenting close to the body an antisymmetrical distribution of vorticity relative to the midspan point.

For sufficiently long cylinders, regimes involving bending oscillations emerge, featuring vibration patterns resembling the structural modes for an unsupported beam. As also observed for the RBM regimes, the horizontal responses are much larger than the vertical ones, and the body deforms periodically, essentially in the horizontal plane, as a standing wave. The associated wake presents a cellular structure, the cells being delimited by the horizontal deformation nodes. Within each cell, two counter-rotating vortex rows globally parallel to the cylinder axis are shed per oscillation cycle. Flow velocity fluctuations are in phase opposition on each side of the deformation nodes, displaying along the cylinder span an alternation of negative and positive vortices. As for the RBM regimes, the intensity of flow unsteadiness tends to drop near the body ends.

For both RBM and BO configurations, the spatio-temporal analysis of the body behaviour and of the surrounding 3-D flow revealed fluid–body synchronization, body motion and flow unsteadiness being both temporally and spatially locked. Temporal synchronization at each spanwise position occurs at a strongly dominant frequency that departs slightly from the vortex shedding frequency known for fixed infinitely long cylinders, and in the case of BO regimes, that also deviates slightly from the natural frequency of the structure. Phase analysis showed that body motion and flow unsteadiness are also locked spatially to each other. The alternating shed vortices are in phase along a portion of the span about the midspan point in the TRA regime, and in phase opposition on each side of the body in the AZI regime: they match the body response phasing. For BO cases, the phases of the horizontal body and fluid fluctuations are a constant piecewise function along the cylinder span, with π jumps between successive cells: the fluid–body system behaviour bears close resemblance to the TRA regime within a cell, and to the AZI regime in a node section, RBM regimes being yet affected in a stronger manner by end effects. This specific structure of the BO regimes may favour the amplitudes displayed, one order of magnitude larger than those encountered for the RBM regimes, with BO regimes benefiting from the combined action of multiple cells, over a wider spanwise region, and being relatively less impacted by end effects.

**Author ORCIDs.**
- Manuel Lorite-Díez https://orcid.org/0000-0002-7392-8622;
- Patricia Ern https://orcid.org/0000-0002-6431-9083;
- Jérôme Mougel https://orcid.org/0000-0003-4196-6138;
- Rémi Bourguet https://orcid.org/0000-0001-8079-3140.

## Appendix A. Complements on the experimental method

### A.1. *Calibration procedure and image pre-processing*

In order to obtain the calibration function that provides the 3-D position of each particle based on individual camera images (Schanz *et al.* 2012, 2013), a calibration procedure is required. This procedure is carried out in two steps: calibration with a target and self-calibration.

A calibration plate (LaVision ref. 204-15-SSDP) is first immersed in the tank with its main surface perpendicular to the $Z$ coordinate. Its position and orientation have been set carefully to respect the $(X, Y, Z)$ coordinate system during its displacement. In order to cover the entire measurement volume, the calibrated plate is moved along the $Z$ axis using a computer-driven translating stage (1 μm precision); eight positions, separated by 5 mm, are considered. The calibrated plate is covered with a regular pattern of white dots. This pattern is identified by DaVis software, which computes, at each position along the $Z$ axis, the mapping function between the two-dimensional images and the laboratory coordinate system. The 3-D calibration function, obtained by interpolation of the above two-dimensional mapping functions at each calibration position, results in a maximum error close to 0.2 pixel. The spatial resolution and magnification used here are 21.78 pixel mm$^{-1}$. Errors lower than 0.1 pixel are, however, required to use the Shake-The-Box (STB) technique (Wieneke 2008; Schanz *et al.* 2012, 2013). To reach this threshold, a volume self-calibration of uncorrelated images is carried out (Wieneke 2008). The self-calibration is an iterative process that modifies the calibration function in order to reduce the disparity between the real images and the re-projected ones. In the present experiments, the typical disparity reached after self-calibration is around 0.03 pixel.

For each experiment, the recorded images are first pre-processed to increase the signal-to-noise ratio and remove any background effects. Then a new volume self-calibration is carried out on each pre-processed image, in order to correct the differences between the experimental and initial calibration conditions. An optical transfer function (OTF) is then obtained. The OTF takes into account the shape of each tracer particle seen by the cameras, and helps to identify these particles on the successive snapshots; it reduces the occurrence of ghost particles (Schanz *et al.* 2012).

The pre-processed images are used (i) to measure the fluid motion about the cylinder by analysing the trajectory of the seeding particles using the STB technique (§ A.2), and (ii) to capture the structural responses by tomographic reconstruction of the cylinder (§ A.3).
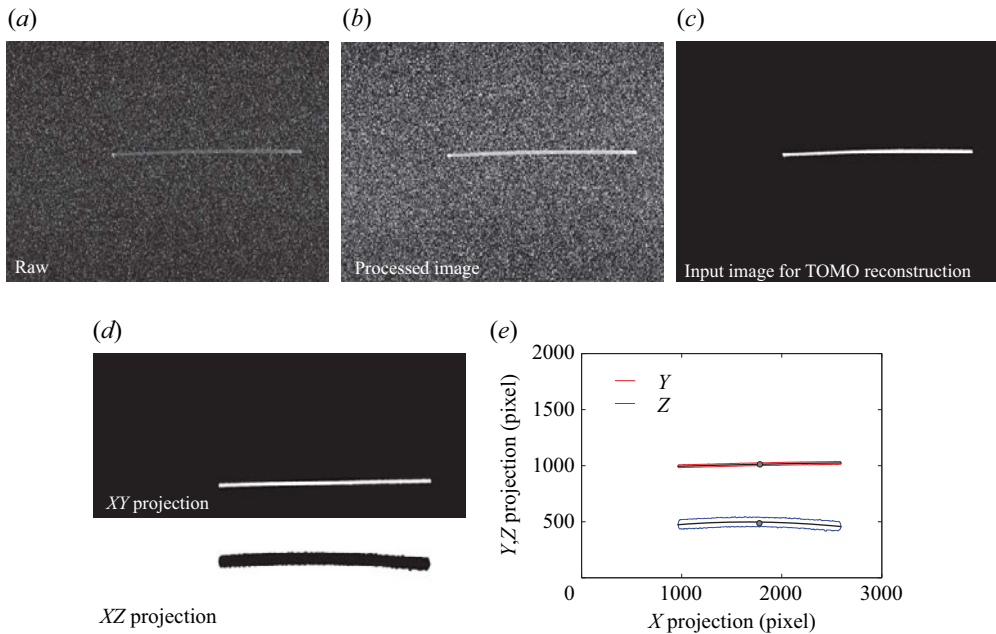
Figure 17. Cylinder reconstruction procedure. (*a*) Raw image recorded by one of the cameras. (*b*) Processed image after log filter. (*c*) Image used for tomographic reconstruction. (*d*) $(X, Y)$ and $(X, Z)$ projections obtained from tomographic reconstruction. (*e*) Cylinder contours on both projection planes, along with cylinder centreline and centre of mass.

### A.2. *Additional details concerning the STB technique*

The STB procedure is applied to the pre-processed images using 5 time steps for the initial phase (IPR and convergence), with a threshold of particle triangulation error equal to 1 pixel. The intensity threshold for removing ghost particles is set to 10 % of the average particle intensity. The shaking area is restricted to 0.1 voxels. Finally, the obtained tracks are limited to certain ranges of velocities and accelerations. Velocity limits are set to 12 voxels in the $X$ and $Z$ directions, and 24 voxels in the $Y$ direction. For the acceleration, the change in particle shift is restricted to an absolute value of 1 voxel and a relative value of 40 %. In a typical case, around 80 000 particles are tracked simultaneously.

### A.3. *Body reconstruction procedure*

In order to determine the dynamics of the cylinder, the recorded images are processed to separate the tracers from the cylinder. First, a logarithm function is applied to the raw images presented in figure 17(*a*) to set all the pixel intensities in a common range (figure 17*b*). After binarization, different operations (mainly morphological) are applied to the images to extract the cylinder contour (figure 17*c*). These processed images are used to obtain the Cartesian re-projections of the cylinder in the $(X, Y)$, $(Y, Z)$ and $(X, Z)$ planes (figure 17*d*). To do so, classical tomographic reconstruction methods such as multiplicative line-of-sight (MLOS) and multiplicative algebraic reconstruction techniques (MART) (Scarano 2012), implemented in LaVision DaVis, are employed.

In order to optimize wake detection in the vertical direction and to cover the entire cylinder span, the four cameras have been placed in a vertical plane. This arrangement causes an overestimation of the cylinder size in the $Z$ direction

(Adhikari & Longmire 2012). This effect has no impact on the results since the cylinder dynamics is determined based on the cylinder centreline, obtained from the upper and lower boundaries of the reconstructed body (figure 17*e*). The accuracy of the present approach was verified by comparison to the results issued from 3-D trajectography with telecentric lenses, for the same cylinders (Ern *et al.* 2020). The cylinder contour projections are also used to determine the coordinates of its centre of mass, $(X_{CM}, Y_{CM}, Z_{CM})$.

REFERENCES

ADHIKARI, D. & LONGMIRE, E.K. 2012 Visual hull method for tomographic PIV measurement of flow around moving objects. *Exp. Fluids* **53**, 943–964.

ANDERSEN, A., PESAVENTO, U. & WANG, Z.J. 2005 Unsteady aerodynamics of fluttering and tumbling plates. *J. Fluid Mech.* **541**, 65–90.

AUGUSTE, F., MAGNAUDET, J. & FABRE, D. 2013 Falling styles of disks. *J. Fluid Mech.* **719**, 388–405.

BOERSMA, P.R., ZHAO, J., ROTHSTEIN, J.P. & MODARRES-SADEGHI, Y. 2021 Experimental evidence of vortex-induced vibrations at subcritical Reynolds numbers. *J. Fluid Mech.* **922**, R3.

BOURGUET, R. 2020 Vortex-induced vibrations of a flexible cylinder at subcritical Reynolds number. *J. Fluid Mech.* **902**, R3.

BOURGUET, R., KARNIADAKIS, G. & TRIANTAFYLLOU, M. 2011*a* Vortex-induced vibrations of a long flexible cylinder in shear flow. *J. Fluid Mech.* **677**, 342–382.

BOURGUET, R., MODARRES-SADEGHI, Y., KARNIADAKIS, G.E. & TRIANTAFYLLOU, M.S. 2011*b* Wake–body resonance of long flexible structures is dominated by counter-clockwise orbits. *Phys. Rev. Lett.* **107**, 134502.

BUFFONI, E. 2003 Vortex shedding in subcritical conditions. *Phys. Fluids* **15**, 814–816.

CHAPLIN, J.R., BEARMAN, P.W., HUERA-HUARTE, F.J. & PATTENDEN, R.J. 2005 Laboratory measurements of vortex-induced vibrations of a vertical tension riser in a stepped current. *J. Fluids Struct.* **21**, 3–24.

CHOW, A.C. & ADAMS, E.E. 2011 Prediction of drag coefficient and secondary motion of free-falling rigid cylindrical particles with and without curvature at moderate Reynolds number. *ASCE J. Hydraul. Engng* **137** (11), 1406–1414.

CHRUST, M., BOUCHET, G. & DUŠEK, J. 2013 Numerical simulation of the dynamics of freely falling discs. *Phys. Fluids* **25**, 044102.

COSSU, C. & MORINO, L. 2000 On the instability of a spring-mounted circular cylinder in a viscous flow at low Reynolds numbers. *J. Fluids Struct.* **14** (2), 183–196.

DAHL, J.M., HOVER, F.S., TRIANTAFYLLOU, M.S. & OAKLEY, O.H. 2010 Dual resonance in vortex-induced vibrations at subcritical and supercritical Reynolds numbers. *J. Fluid Mech.* **643**, 395–424.

DOLCI, D.I. & CARMO, B.S. 2019 Bifurcation analysis of the primary instability in the flow around a flexibly mounted circular cylinder. *J. Fluid Mech.* **880**, R5.

ERN, P., MOUGEL, J., CAZIN, S., LORITE-DÍEZ, M. & BOURGUET, R. 2020 Bending oscillations of a cylinder freely falling in still fluid. *J. Fluid Mech.* **905**, R5.

ERN, P., RISSO, F., FABRE, D. & MAGNAUDET, J. 2012 Wake-induced oscillatory paths of bodies freely rising or falling in fluids. *Annu. Rev. Fluid Mech.* **44**, 97–121.

FABRE, D., ASSEMAT, P. & MAGNAUDET, J. 2011 A quasi-static approach to the stability of the path of heavy bodies falling within a viscous fluid. *J. Fluids Struct.* **27**, 758–767.

FAN, D., WANG, Z., TRIANTAFYLLOU, M.S. & KARNIADAKIS, G.E. 2019 Mapping the properties of the vortex-induced vibrations of flexible cylinders in uniform oncoming flow. *J. Fluid Mech.* **881**, 815–858.

FERNANDES, P.C., RISSO, F., ERN, P. & MAGNAUDET, J. 2007 Oscillatory motion and wake instability of freely rising axisymmetric bodies. *J. Fluid Mech.* **573**, 479–502.

GEDIKLI, E.D., CHELIDZE, D. & DAHL, J.M. 2018 Observed mode shape effects on the vortex-induced vibration of bending dominated flexible cylinders simply supported at both ends. *J. Fluids Struct.* **81**, 399–417.

HOROWITZ, M. & WILLIAMSON, C. 2006 Dynamics of a rising and falling cylinder. *J. Fluids Struct.* **22**, 837–843.

HOROWITZ, M. & WILLIAMSON, C.H.K. 2010 Vortex-induced vibration of a rising and falling cylinder. *J. Fluid Mech.* **662**, 352.

HUERA-HUARTE, F.J. & BEARMAN, P.W. 2009 Wake structures and vortex-induced vibrations of a long flexible cylinder – Part 1: dynamic response. *J. Fluids Struct.* **25** (6), 969–990.

INOUE, O. & SAKURAGI, A. 2008 Vortex shedding from a circular cylinder of finite length at low Reynolds numbers. *Phys. Fluids* **20** (3), 033601.

JAYAWEERA, K.O.L.F. & MASON, B.J. 1965 The behaviour of freely falling cylinders and cones in a viscous fluid. *J. Fluid Mech.* **22** (4), 709–720.

JEONG, J. & HUSSAIN, F. 1995 On the identification of a vortex. *J. Fluid Mech.* **285**, 69–94.

KARNIADAKIS, G.E. & TRIANTAFYLLOU, G.S. 1992 Three-dimensional dynamics and transition to turbulence in the wake of bluff objects. *J. Fluid Mech.* **238**, 1–30.

KRAMER, O.J.I., DE MOEL, P.J., RAAGHAV, S.K.R., BAARS, E.T., VAN VUGT, W.H., BREUGEM, W.-P., PADDING, J.T. & VAN DER HOEK, J.P. 2021 Can terminal settling velocity and drag of natural particles in water ever be predicted accurately? *Drink. Water Engng Sci.* **14** (1), 53–71.

LAU, E.M., ZHANG, J.D., JIA, Y.X., HUANG, W.X. & XU, C.X. 2019 Vortical structures in the wake of falling plates. *J. Vis.* **22**, 15–24.

MARCHILDON, E.K., CLAMEN, A. & GAUVIN, W.H. 1964 Drag and oscillatory motion of freely falling cylindrical particles. *Can. J. Chem. Engng* **42** (4), 178–182.

MATHAI, V., ZHU, X., SUN, C. & LOHSE, D. 2017 Mass and moment of inertia govern the transition in the dynamics and wakes of freely rising and falling cylinders. *Phys. Rev. Lett.* **119**, 054501.

MELIGA, P. & CHOMAZ, J.-M. 2011 An asymptotic expansion for the vortex-induced vibrations of a circular cylinder. *J. Fluid Mech.* **671**, 137–167.

MITTAL, S. & SINGH, S. 2005 Vortex-induced vibrations at subcritical *Re*. *J. Fluid Mech.* **534**, 185–194.

NAMKOONG, K., YOO, J.Y. & CHOI, H.G. 2008 Numerical analysis of two-dimensional motion of a freely falling circular cylinder in an infinite fluid. *J. Fluid Mech.* **604**, 33–54.

NEWMAN, D.J. & KARNIADAKIS, G.E. 1997 A direct numerical simulation study of flow past a freely vibrating cable. *J. Fluid Mech.* **344**, 95–136.

PAÏDOUSSIS, M.P., PRICE, S.J. & DE LANGRE, E. 2010 *Fluid–Structure Interactions: Cross-Flow-Induced Instabilities*. Cambridge University Press.

PESAVENTO, U. & WANG, Z.J. 2004 Falling paper: Navier–Stokes solutions. Model of fluid forces, and center of mass elevation. *Phys. Rev. Lett.* **93**, 144501.

RAMBERG, S.E. & GRIFFIN, O.M. 1974 Vortex formation in the wake of a vibrating, flexible cable. *J. Fluids Engng* **96** (4), 317–322.

ROMERO-GOMEZ, P. & RICHMOND, M.C. 2016 Numerical simulation of circular cylinders in free-fall. *J. Fluids Struct.* **61**, 154–167.

ROSHKO, A. 1993 Perspectives on bluff body aerodynamics. *J. Wind Engng Ind. Aerodyn.* **49** (1–3), 79–100.

SARPKAYA, T. 2004 A critical review of the intrinsic nature of vortex-induced vibrations. *J. Fluids Struct.* **19** (4), 389–447.

SAVITZKY, A. & GOLAY, M.J.E. 1964 Smoothing and differentiation of data by simplified least squares procedures. *Anal. Chem.* **36** (8), 1627–1639.

SCARANO, F. 2012 Tomographic PIV: principles and practice. *Meas. Sci. Technol.* **24** (1), 012001.

SCHANZ, D., GESEMANN, S. & SCHRÖDER, A. 2016 Shake-The-Box: Lagrangian particle tracking at high particle image densities. *Exp. Fluids* **57** (5), 70.

SCHANZ, D., GESEMANN, S., SCHRÖDER, A., WIENEKE, B. & NOVARA, M. 2012 Non-uniform optical transfer functions in particle imaging: calibration and application to tomographic reconstruction. *Meas. Sci. Technol.* **24** (2), 024009.

SCHANZ, D., SCHRÖDER, A., GESEMANN, S., MICHAELIS, D. & WIENEKE, B. 2013 Shake-The-Box: a highly efficient and accurate tomographic particle tracking velocimetry (TOMO-PTV) method using prediction of particle positions. In *10th International Symposium on Particle Image Velocimetry, Delft, The Netherlands*. Delft University of Technology.

SEYED-AGHAZADEH, B., EDRAKI, M. & MODARRES-SADEGHI, Y. 2019 Effects of boundary conditions on vortex-induced vibration of a fully submerged flexible cylinder. *Exp. Fluids* **60**, 38.

SINGH, S.P. & MITTAL, S. 2005 Vortex-induced oscillations at low Reynolds numbers: hysteresis and vortex-shedding modes. *J. Fluids Struct.* **20**, 1085–1104.

TCHOUFAG, J., FABRE, D. & MAGNAUDET, J. 2014 Global linear stability analysis of the wake and path of buoyancy-driven disks and thin cylinders. *J. Fluid Mech.* **740**, 278–311.

TOUPOINT, C., ERN, P. & ROIG, V. 2019 Kinematics and wake of freely falling cylinders at moderate Reynolds numbers. *J. Fluid Mech.* **866**, 82–111.

WIENEKE, B. 2008 Volume self-calibration for 3D particle image velocimetry. *Exp. Fluids* **45** (4), 549–556.

WIENEKE, B. 2012 Iterative reconstruction of volumetric particle distribution. *Meas. Sci. Technol.* **24** (2), 024008.

WILL, J.B. & KRUG, D. 2021 Rising and sinking in resonance: mass distribution critically affects buoyancy-driven spheres via rotational dynamics. *Phys. Rev. Lett.* **126**, 174502.

WILL, J.B., MATHAI, V., HUISMAN, S.G., LOHSE, D., SUN, C. & KRUG, D. 2021 Kinematics and dynamics of freely rising spheroids at high Reynolds numbers. *J. Fluid Mech.* **912**, A16.

WILLIAMSON, C.H.K. 1989 Oblique and parallel modes of vortex shedding in the wake of a circular cylinder at low Reynolds numbers. *J. Fluid Mech.* **206**, 579–627.

WILLIAMSON, C.H.K. 1996 Vortex dynamics in the cylinder wake. *Annu. Rev. Fluid Mech.* **28**, 477–539.

WILLIAMSON, C.H.K. & BROWN, G.L. 1998 A series in $1/\sqrt{Re}$ to represent the Strouhal–Reynolds number relationship of the cylinder wake. *J. Fluids Struct.* **12** (8), 1073–1085.

WILLIAMSON, C.H.K. & GOVARDHAN, R. 2004 Vortex-induced vibrations. *Annu. Rev. Fluid Mech.* **36**, 413–455.

WU, X., GE, F. & HONG, Y. 2012 A review of recent studies on vortex-induced vibrations of long slender cylinders. *J. Fluids Struct.* **28**, 292–308.

ZHANG, H.-Q., FEY, U., NOACK, B.R., KÖNIG, M. & ECKELMANN, H. 1995 On the transition of the cylinder wake. *Phys. Fluids* **7** (4), 779–794.